Diss. ETH No. 10780

Proton Radiography: A tool for quality control in proton therapy

A dissertation submitted to the
EIDGENÖSSISCHE TECHNISCHE HOCHSCHULE ZÜRICH
SWISS FEDERAL INSTITUTE OF TECHNOLOGY ZÜRICH

for the degree of

Doktor der Naturwissenschaften
Doctor of Natural Sciences

presented by

Uwe Schneider
Dipl. Phys. of the Universität Bayreuth
born February 2, 1964
from Spielberg in Franken, Bayern/Bavaria

accepted on the recommendation of

Prof. Dr. Max Anliker	examiner
Prof. Dr. Peter Rüegsegger	co-examiner
Dr. Eros Pedroni	co-examiner

This work was performed at the Department of Radiation Medicine at the Paul Scherrer Institute in Villigen, Switzerland. The author is grateful for its kind hospitality, and to the PSI and the Schweizerische Krebsliga for financial support.

1994

Dedicated to those who can understand this dedication:

Dou moina allerweil die Leid:
Wer Bäicher schreibd der is rechd gscheid.
I hob scho manchmal Bäicher glesn,
Dou is a schäiner Schmarrn drin gwesen.
Wos s'dou drin ofd alls zamma läign,
Dou koarsd fasd an Herzkaschber gräign.
I ho mir zwoar des meina dengd
Und solche Bäicher weider gschengd.
Des Boach dou hob i bhaldn mäin,
Kaa Wunner - hob's aa selber gschriebn.
An jedn indressierds edz gwiess,
Wäis überhabd endschdandn is.
Aus diesem Grund und weils mi freid
Kommd nu a Verserl was sich reimd.

Manchmal houd's scho an Guggugg gsehgn,
Wenn'sd irgend surra hards Broblem,
A Rädsl odder sunsd a Ding,
Mogsd aassergraign - ja, Bfifferling!!
Es gäid niad aaf - waisd aa schdudiersd
Und Dooch und Nachd droa hiesinniersd.
Es is nadürlich mehr bequem,
Wenn sd' lebsd und denggsd an kaa Broblem.
Und doch gibbs Frougn die wo di druggn,
Gour maansd, du hoasd im Hirn a Luggn.
Und däi mogsd zugräign irchendwie,
Bei mir woars hald d' *Brodonenradiografie.*

Aus dem Broblem, ma solld's ned glaam,
Dou is des ganze Bouch draus worn.
Grood einfach woars niad zum derzülln,
Denn schdimma solls und nix derf fölln.
I hoff Ihr seids mir aa niad bäiss,
Dass des Bouch aaf Englisch is.
An Vordeil houds, für jedn Frank,
Es is niad preissisch, Godd sei Dank!

Abstract

In this work the feasibility of proton radiography as a tool in proton therapy is studied.

In the first part the particular problem of spatial resolution in proton radiography is presented. A simple formula for the spatial resolution of transmission proton radiography is derived for different methods of measuring the proton coordinates. The effect of multiple Coulomb scattering and energy loss are taken into account. Experimental measurements of the spatial resolution have been done and are compared with the calculations. The technique of measuring entrance and exit coordinates in coincidence for each single proton improves the spatial resolution by a factor five compared to a single coordinate measurement. An additional measurement of the protons incident angle and exit angle increases the resolution by eight times.

In the second section proton radiography is investigated for its use as a quality control tool in proton therapy. Images were produced both with range and range uncertainty information of protons passing through phantoms (Alderson phantom and a sheep's head). With the range images the correct positioning of the patient with respect to the beam could be verified. The range uncertainty images were used to quantitatively detect range variations of protons passing through inhomogeneities in the patient. These measurements can be used to indicate critical situations during proton therapy or to determine the safety margin around the tumour volume. With the range information the precision of different calibrations of CT-Hounsfield values to relative proton stopping power, used for proton treatment planning, was determined. It is found that the precision in range can be improved by a detailed analysis of the calibration data obtained from tissue-substitute measurements, by a factor of 2.5. The resulting range errors are in the order of the positioning precision.

Zusammenfassung

In der vorliegenden Arbeit werden die Möglichkeiten für den Einsatz der Protonenradiographie als ein Hilfsmittel für die Protonentherapie diskutiert.

Im ersten Teil wird das Problem der Ortsauflösung in der Protonenradiographie ausführlich behandelt. Einfache analytische Formeln, welche die Ortsauflösung in der Transmissionsprotonenradiographie für verschiedene Arten der Protonenkoordinatenmessung beschreiben, werden abgeleitet. Es wird der Einfluss der Vielfachstreuung und des Energieverlustes der Protonen in Materie auf die Ortsauflösung betrachtet. Es wurden Experimente zur Messung der Ortsauflösung durchgeführt und die Ergebnisse mit den Rechnungen verglichen. Die Messtechnik, bei welcher die Eintritts- und die Austrittskoordinate für jedes einzelne Proton in Koinzidenz gemessen wird, verbessert die Ortsauflösung, verglichen mit einer Einzelkoordinatenmessung, um einen Faktor fünf. Werden zusätzlich Ein- und Ausfallswinkel für einzelne Protonen gemessen kann die Ortsauflösung um den Faktor acht verbessert werden.

Im zweiten Teil der Arbeit wurde untersucht, inwieweit die Protonenradiographie zur Qualitätskontrolle in der Protonentherapie eingesetzt werden kann. Es wurden aus der Reichweiteninformation und der Reichweitenunsicherheitsinformation von Protonen, die durch verschiedene Phantome (Alderson Phantom und Schafskopf) drangen, Radiographiebilder erzeugt. Mit Hilfe der Reichweitenbilder konnte die korrekte Positionierung des Patienten, anhand von Phantommessungen, im Strahl verifiziert werden. Die Reichweitenunsicherheitsbilder wurden verwendet, um Reichweitenfehler, die aus der Wechselwirkung der Protonen mit Inhomogenitäten im Patienten resultieren, zu messen und zu quantifizieren. Diese Messungen können verwendet werden, um kritische Situationen in der Protonentherapie anzuzeigen oder Sicherheitsmargen um das Tumorvolumen zu definieren. Mit den Reichweitenbildern wurde die Genauigkeit von verschiedenen Kalibrationen, welche CT-Hounsfield Werte in wasseräquivalente Länge transformieren und in der Protonentherapie verwendet werden, überprüft und verbessert. Es wurde herausgefunden, daß aufgrund von Messungen gewebeäquivalenter Proben die Reichweitenpräzision durch eine detailierte Analyse der gemessenen Kalibrationskurven um einen Faktor 2.5 verbessert werden kann. Die resultierenden Reichweitenfehler liegen in der Grössenordnung der Positionierungsgenauigkeit.

Contents

List of Figures

List of Tables

1. Motivation

Proton radiography and tomography as a diagnostic tool was investigated (Hanson et al. 1981, Hanson et al. 1982, Mofett et al. 1975, Koehler and Steward 1973ab) in the early 1970's but was more or less abandoned due to the success of x-ray computed tomography. However interest in proton radiography is now growing in the light of the increasing success of proton radiotherapy which seems to be one of the most promising improvements to conventional treatments using photons and electrons.

Due to their well defined range in tissue, protons deposit most of their energy at the end of the range, in the so called Bragg peak (figure 1). Compared to photons, which are characterised by an exponential dose fall-off with depth, the proton dose in front of the Bragg peak shows a moderate entrance dose, followed by the Bragg peak itself with essentially zero dose beyond the Bragg peak. This advantage can be used to irradiate tumours in the proximity of sensitive healthy structures. The indications include, for example, precision treatments of tumours at the base of the skull or close to the spinal cord. The described characteristics of proton therapy result in a dose reduction outside the target volume by a factor of 2 to 5 compared to photons (Archambeau et al. 1974). Protons, due to their excellent localisation in space are also well suited for the conformal irradiation of large irregular target volumes.

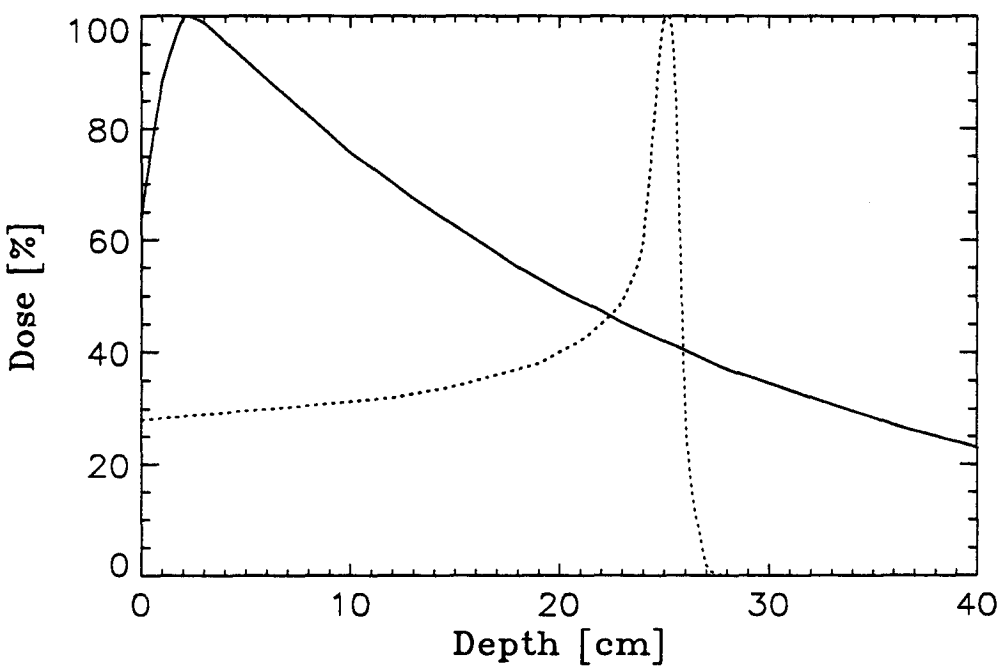

Figure 1 Deposited dose in water as a function of depth. The solid line represents the dose of 25 MV photons, the dotted line the dose deposition of 200 MeV protons.

In addition protons, which are charged particles, can be scanned as pencil beams using magnetic fields under computer control. With this method the dose can be tailored exactly to the tumour (Pedroni et al. 1989-92, Pedroni and Enge 1993). This approach to proton therapy, the so called spot scanning technique, is presently being developed at the Paul Scherrer Institute (PSI) (Pedroni et al. 1994). As a part of this project an isocentric gantry is being built at PSI to make use of the full advantage of multiple field therapy as used routinely in conventional photon or electron therapy.

The aim of this thesis is to study the feasibility of a proton radiographic system for the quality control of proton therapy. The thesis is devided in two sections.

In the first section[1] (chapter 2), the spatial resolution of proton radiographic systems is studied in detail. Measurements and analytical calculations were done to examine the influence of different measurement techniques on the spatial resolution. It is found that for both quality control and diagnostics purposes a sufficent spatial resolution can be achieved.

In the second section[2] (chapter 3), experiments are described to determine whether proton radiography is useful for checking calculated dose distributions. We report on studies of direct measurements of the proton range and of range uncertainties for single protons which pass through inhomogeneous tissue. These measurements where compared to calculations of proton ranges based on an algorithm used for proton treatment planning. This comparison gives information about the validity of predicted dose distributions and may help to improve the precision of proton therapy. In addition the possibility of verifying the patient's position with respect to the treatment beam using proton images was experimentally investigated. We conclude from the second section that proton radiography has the ability to precisely measure the range and range variations in vivo and to detect errors in the predicted proton ranges. The position verification of a patient before and after treatment can be achieved with a precision similar to the voxel size of the reconstructed image.

[1] Submitted to Medical Physics (Schneider and Pedroni 1993), accepted: June 23, 1994.

[2] Submitted to Medical Physics (Schneider and Pedroni 1994)

2. Multiple Coulomb Scattering and Spatial Resolution in Proton Radiography

2.1 Introduction

The utility of proton radiography and proton tomography for both diagnostic and quality control purposes should be investigated from the point of view of the increased availability of proton sources with adequate energy in the future. Proton diagnostic images are characterized by a high density resolution with a very low dose to the patient. The main disadvantage is the poor spatial resolution compared to conventional x-ray images.

The limiting factor affecting position resolution is given by the multiple Coulomb scattering (mcs) of the protons in the patient. Protons undergo numerous small angle deflections caused by their interaction with the Coulomb field of the nuclei of the traversed material, which produces uncertainties in the reconstructed trajectory.

To reduce the position uncertainty caused by mcs, one can measure the entry point *A* of the proton when it penetrates into the material and also the exit point *B* where it leaves the material (see figure 2). In addition it is also possible to measure the entrance and exit angles of single protons before entering and after leaving the sample. In sections 2.3 and 2.4 we study the consequence of measuring the entry and exit points on spatial resolution and in section 2.5 we will investigate also the angle measurement case. There are in principle two possibilities for measuring *A* and *B*. The protons which are entering and leaving through fixed points *A* and *B* will be detected using collimators. As an alternative one can measure point *A* with a collimator and *B*, for example, with a Multiwire Proportional Chamber (MWPC), or alternatively both points with MWPCs. The data can be analyzed in terms of a fixed entrance point *A* and a unconstrained ("free") measured exit point *B*. In this chapter we present the results of the calculated spatial resolution as a function of depth in the sample for these techniques and we compare them with experimental results.

The formulae of this section are derived for the coincidence technique taking into account the effects of energy loss. Rossi and Greisen (1941) have calculated the distribution function for the lateral and angular displacements of protons which undergo multiple elastic scattering, for the case when *A* and *B* are fixed and have no defined incident phase space. Their calculation did not include the energy loss in the material and was not performed for an incident pencil beam of known direction. Highland (1975), Mustafa and Jackson (1981), Bichsel et al. (1982) and Lynch and Dahl (1991) gave some corrections to Rossi's formula , but did not include the investigation of the particular problem of the coincidence measurement through two points *A* and *B*, which is important for proton radiography.

We have performed experimental work on proton radiography as a feasibility study for its implementation on the PSI compact gantry. In this section we investigate the sepa-

rate problem of the effect of multiple Coulomb scattering on the spatial resolution of proton radiography.

2.2 Experimental setup

The purpose of the experimental apparatus was to collect the information necessary to simulate all the mentioned different methods for producing radiographic images without attempt to speed up the collection time of data. This problem will be considered for the choice of the design of the final apparatus. The experimental set-up depicted in figure 2 was placed in the proton therapy beamline (NA3) of PSI. The beam we used had a spot 10.5 mm (FWHM) wide by 13.6 mm (FWHM) high. Every proton was first detected in a position sensitive proportional chamber (MWPC1) with wire spacing of 2 mm in front of the sample. On exiting the phantom the protons were detected in a second chamber (MWPC2), then in a scintillation counter and finally in a NaI detector where it was stopped. The signal from the scintillation counter was taken in coincidence with the two multiwire chambers and the NaI to form an event for the data taking system. Radiographic images were produced by scanning the sample in both directions transverse to the beam. Data taking was accomplished by means of standard CAMAC[11] modules read-out by a Starburst computer[12]. The present data taking system permitted only an average rate of 1000 events per second. The Starburst transferred unprocessed event data as well as phantom position information to a VAXstation[13].

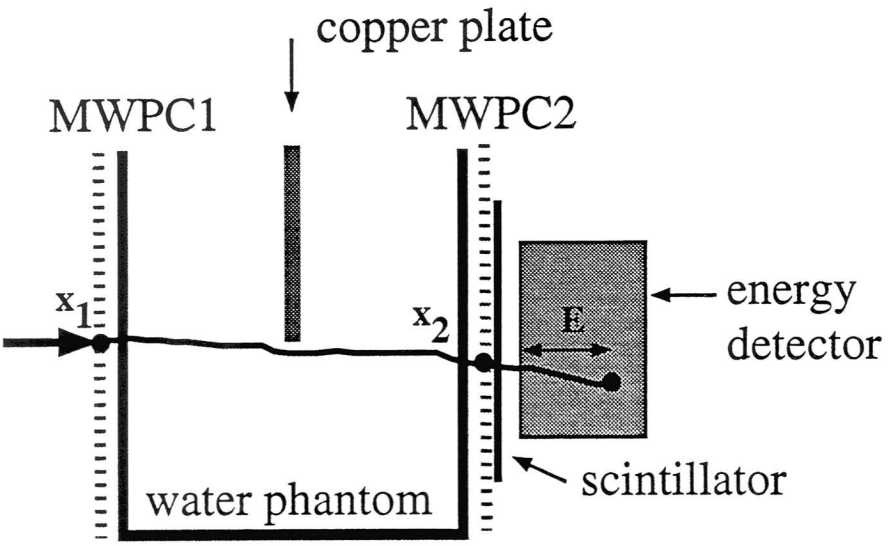

Figure 2 Experimental set-up for the measurement of the spatial resolution (MWPCs are multi wire proportional chambers).

[11] IEEE Standards 583 and 596

[12] Creative Electronic Systems S.A.

[13] Digital Equipment Corporation

In the analysis, carried out on a VAXstation, the spatial information of the two wire chambers was used to reconstruct the intercepts of the (most likely) proton trajectory of every event with equally spaced parallel planes between MWPC1 and MWPC2. The intercept coordinates were used as the pixel addresses (minimum size: 1 mm) of the images reconstructed at different depths in the phantom, as a mean to better resolve structures located at that depth (Appendix C). The average value of the NaI energy spectrum for each pixel determined the mean residual range of the protons, which represents the pixel value shown in the images.

We scanned with this method a homogeneous water phantom with copper plates located at different depths. By fitting an error-function to the measured energy fall-off caused by the edge of the copper plate we obtained the spatial resolution. The RMS spatial resolution of the MWPCs has been subtracted from the measured values before comparing it with the analytical calculations.

2.3 The scattering process

The calculation model is a modification of Fermi's theory (Rossi and Greisen 1941, Rossi 1965) of the scattering process which results in a Gaussian approximation for small angles. In our notation the projected distribution function $f(t,x,\theta)$ is given as

$$f(t,x,\theta)\,dxd\theta = \frac{1}{\pi\sqrt{D_o^t}}\, e^{\frac{-A_o^t\theta^2+2B_o^t x\theta-C_o^t x^2}{D_o^t}}\, dxd\theta \qquad (1)$$

where $f(t,x,\theta)$ is the probability that a proton undergoing multiple scattering in a homogeneous material of thickness $z = tR$ along the z-axis will be emitted at a projected angle θ in the x,z-plane and at a projected displacement x at z, where R is the range of the protons in the material and t is the traversed thickness measured as a fraction of the initial range. The coefficient $D^t_o = A^t_o C^t_o - B^{t\,2}_o$ is a function of all the other coefficients. If we integrate over x we get the angular distribution irrespective of displacement and if we integrate over θ we get the lateral distribution independent of angle. We see that the standard deviations for x and θ are

$$\sigma_x(t) = \sqrt{\frac{A_o^t}{2}}, \qquad \sigma_\theta(t) = \sqrt{\frac{C_o^t}{2}}\,. \qquad (2)$$

The transport equations for the coefficients *A*, *B* and *C* through the material are given by the following integrals:

$$A_{t_1}^{t_2} = R^3 \int_{t_1}^{t_2} \theta_u(E(\tilde{t}))^2 (t_2 - t_1 - \tilde{t})^2 \, d\tilde{t} \ , \tag{3}$$

$$B_{t_1}^{t_2} = R^2 \int_{t_1}^{t_2} \theta_u(E(\tilde{t}))^2 (t_2 - t_1 - \tilde{t}) \, d\tilde{t} \ , \tag{4}$$

$$C_{t_1}^{t_2} = R \int_{t_1}^{t_2} \theta_u(E(\tilde{t}))^2 \, d\tilde{t} \ . \tag{5}$$

where $\theta_u(E)$ represents the amount of scattering ($\sigma\sqrt{2}$) per unit length of material traversed. If the material is homogeneous the only dependence of θ_u in depth is given by the energy $E(t)$. We follow the method described by Øverhås (1960) who introduced the dependence on the energy slowdown through the empirical formula

$$\theta_u(t) = \frac{\theta_s}{(1-t)^{(1+k)/2}} \ , \tag{6}$$

where k is a material dependent number (k=0.074 for water) which is much smaller than unity and θ_s is the contribution to the mcs angle per unit length at the entrance energy. We use

$$\theta_s = \frac{E_s}{p\beta c} \sqrt{\frac{\rho}{L_{rad}}} \ , \tag{7}$$

where p and β c are the momentum and velocity of the scattered particle and L_{rad} denotes the radiation length. This is given by

$$\frac{1}{L_{rad}} = \frac{4\alpha N_a}{A} Z(Z+1) r_e^2 \ ln(183 Z^{-1/3}) \ . \tag{8}$$

We neglect in the formula for the scattering angle the logarithmic term, which is usually used (Highland 1975, Lynch and Dahl 1991) for the calculation of samples of finite thickness. It is not clear to us if and how this term should be treated in the integration. Instead of E_s=13.6 $\sqrt{2}$ MeV the value of E_s= 18 MeV has been used in our calculation. This value was found to produce the best fit to the mcs modification of the width

of a proton pencil beam measured with small ionization chambers in a water bath (Scheib 1994).

2.4 Coincidence through two fixed points on the beam axis

We consider the case of a proton pencil beam traversing a material sample. The entrance and exit points of the beam axis define A and B respectively. In this section we will calculate the spatial resolution which can be achieved when considering protons leaving through a small collimator placed at point B. First, consider an arbitrary point D that lies in the exit plane and is displaced by distance x_D from point B. For protons exiting the sample at point D the sidewise distribution of the trajectories at any depth between A and B can be calculated. Let us take A as the origin of the system of coordinates and AB as the z-axis (figure 3). We draw a straight line perpendicular to the segment AB at the depth t and consider a point C of this line at a distance x_t from the axis. The protons are incident at A in the direction of the z axis. For the sake of simplicity we consider the case where the proton range corresponds to the distance AB.

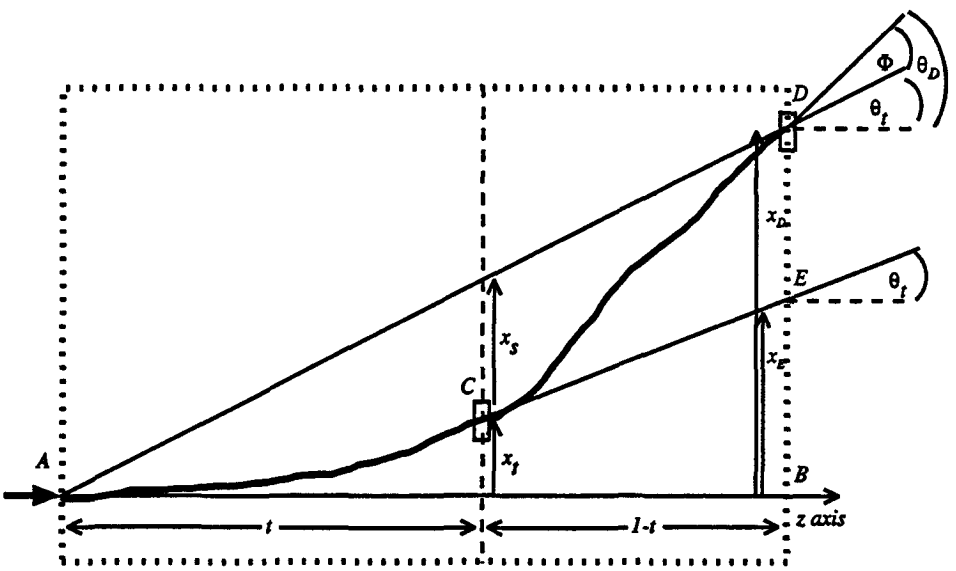

Figure 3 Illustration of the calculation of the sidewise distribution of protons passing through two points A and D.

The differential probability dP_{AC} to detect a proton inside a small given interval Δx_t around point C and with an angle θ_t is

$$dP_{AC} = f(t, x_t, \theta_t)\, d\theta_t \Delta x_t \ . \qquad (9)$$

The differential probability for a proton to reach a given exit point D, when starting from point C with an angle θ_t (i.e. again a pencil beam starting at C) is given by

$$dP_{CD} = f(1-t, x_D - x_E, \phi)\, d\phi\, \Delta x_D \ . \qquad (10)$$

Note that this distribution is centered around the point E with $x_E = x_t + \theta_t (1-t) R$ and that we introduced the angle $\phi = \theta_D - \theta_t$. The differential probability to measure protons in coincidence at C and D is the integral over ϕ and θ_t of

$$dP_{ACD} = dP_{AC} dP_{CD} \ . \qquad (11)$$

The result of the integration over ϕ yields

$$\frac{1}{\pi^{3/2}\sqrt{D_o^t A_t^1}} e^{\frac{-A_o^t \theta_t^2 + 2B_o^t x_t \theta_t - C_o^t x_t^2}{D_o^t} - \frac{(x_D - x_t - \theta_t (1-t) R)^2}{A_t^1}} d\theta_t \ . \qquad (12)$$

We now consider the special case where the collimator is placed at B (B is equal to D). With x_D equal to zero the integration over θ_t yields a gaussian distribution in x_t with width σ_{xt}

$$\sigma_{x_t}^2 = \frac{1}{2\left(\frac{\left(\frac{B_o^t}{D_o^t} - \frac{(1-t)R}{A_t^1}\right)^2}{-\frac{A_0^t}{D_o^t} - \frac{(1-t)^2 R^2}{A_t^1}} - \frac{C_o^t}{D_o^t} - \frac{1}{A_t^1} \right)} \ . \qquad (13)$$

Neglecting energy loss and substituting $t = 1/2$ in the expression for σ_{xt}, that is looking for the displacement at half of the distance between A and B, we get

$$\sigma_{x_t}^2 = \frac{7}{1536} \theta_s^2 R^3 \ , \qquad (14)$$

which can be compared with Rossi's (1965) result

$$\sigma_{x_t}^2 = \frac{1}{96}\theta_s^2 R^3 \ . \qquad (15)$$

We obtain a smaller value for the lateral displacement, because our calculation is done for a pencil beam, in contrast to Rossi's computation, which is done for protons, incident at A, uniformly distributed over different directions. As a first conclusion we see that working with a pencil beam of known incident direction improves the spatial resolution by a factor of 1.5. For a more realistic description of the problem we can include the angle distribution of the initial phase space of the beam, into the equations. To this end we extend our formulae (3) to (5) to

$$A_{ini} = 2\sigma_0^2 t^2 R^2 + A_{t_1}^{t_2} \ , \qquad (16)$$

$$B_{ini} = 2\sigma_0^2 tR + B_{t_1}^{t_2} \ , \qquad (17)$$

$$C_{ini} = 2\sigma_0^2 + C_{t_1}^{t_2} \ , \qquad (18)$$

where σ_0 is the variance of the initial angle distribution. As we can see from figure 4

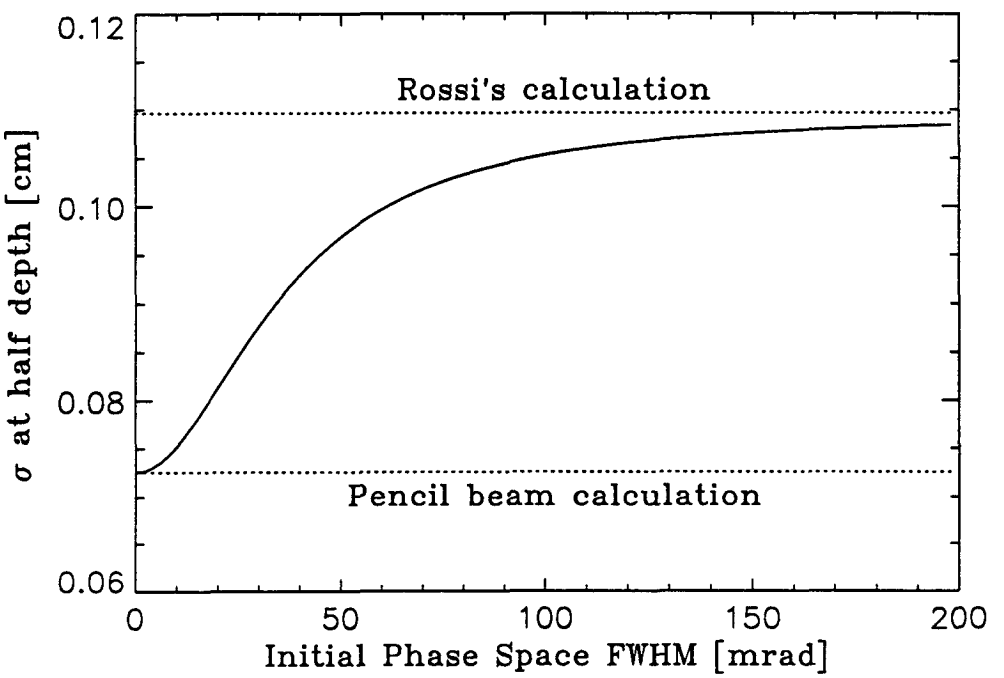

Figure 4 Spatial resolution at half depth as a function of the initial phase space not including energy loss. The dotted lines are Rossi's calculation for protons with a uniform angle distribution and a pencil beam calculation with zero phase space. The solid line is a beam calculation with finite initial phase space.

(as an example for 200 MeV protons in water) with increasing σ_0 the lateral displacement tends towards Rossi's value. The pencil beam calculation is, however, the better choice for phase space distributions up to 15 mrad. We now take the energy loss into account. Using Øverås's formula (6) for the energy dependence of the scattering angle θ we can calculate the coefficients A,B and C in equation (13) as a function of depth. To simplify the expressions an appropriate expansion is:

$$\sigma_{x_t}(t)^2 = \sigma_{x_t}^{2^0} + \sigma_{x_t}^{2^1} k + \sigma_{x_t}^{2^2} k^2 + \cdots \qquad (19)$$

because k in Øverås's equation (6) is much smaller than unity. The resulting function for σ_t is a complex formula. The result for the case of 200 MeV protons in water is shown as a function of the depth as the dotted line in figure 5. In the picture we compare the result of the analytical calculation with our experimental results (squares) performed with protons of slightly higher energy. The agreement between theory and experiment is satisfactory.

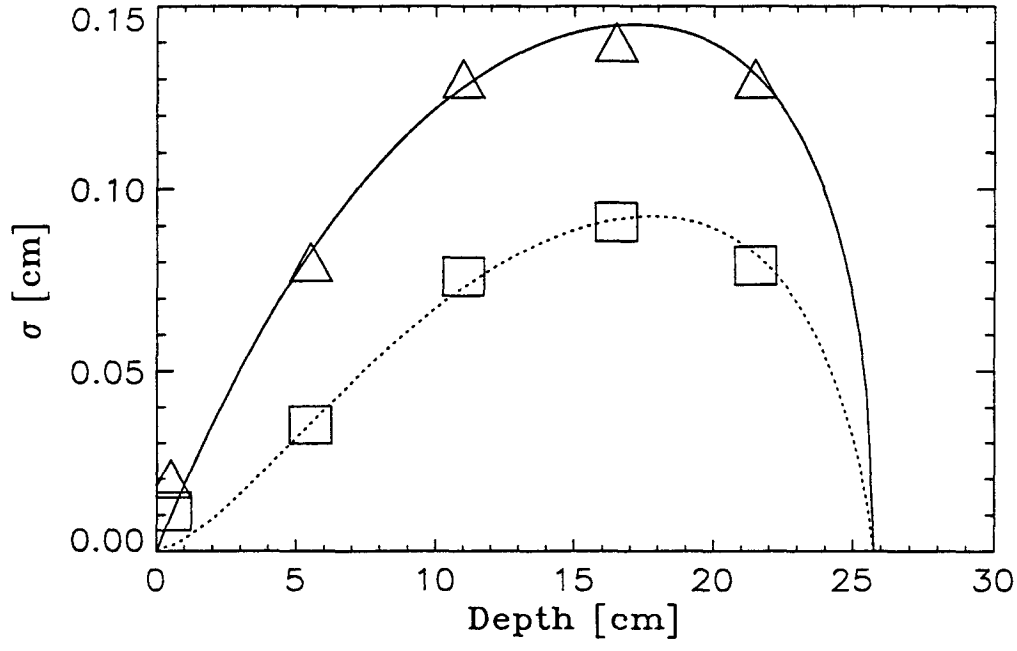

Figure 5 Spatial resolution of 200 MeV protons including energy loss as a function of depth in water. Comparison of the collimator-case (dotted line is the analytical calculation, squares are the measurements) with the straight-line-case (solid line is the analytical calculation, triangles are the measurements).

2.5 Coincidence through a fixed and a free point

We consider next the case where the exit point is measured but not constrained by the experimental apparatus.

We refer again to figure 3. We now draw a straight line from point *A* to point *D*. This line is used for the calculation of the pixel addresses as discussed in section 2.2. The distance of point *C* from this line is defined as x_s. The variance of the distribution of x_s is now proportional to the spatial resolution. As in the previous case x_t and x_D are the distances from the *z* axis of point *C* and *D* respectively. The probability to find a proton at point *C* with θ_t is again given by equation (9). The differential probability to find a proton at a variable point *D* starting from *C* with angle θ_t is again given by equation (10). We are interested in the width of the distribution of the x_s values calculated from x_D. We thus substitute

$$x_D = \frac{x_t + x_s}{t} \quad , \quad dx_D = \frac{1}{t} dx_s \tag{20}$$

in equation (11). If we now integrate equation (11) over θ_t ,ϕ and x_t this yields a gaussian distribution with width σx_s, which is the spatial resolution we are interested in:

$$\begin{aligned} \sigma_{x_s}^2 = \frac{1}{2D_0^t}\Big(& -A_t^1 B_o^{t\,2} t^2 - 2B_o^t D_o^t t(1-t)^2 R + A_t^1 A_o^t C_o^t t^2 \\ & + C_o^t D_o^t t^2 (1-t)^2 R^2 + A_o^t D_o^t (1-t)^2 \Big). \end{aligned} \tag{21}$$

We can calculate A, B and C from formulas (3) to (5) taking into account the energy loss calculated from formula (6). Taking the expansion (19) we obtain the following formula for the spatial distribution as a function of depth up to the $O(k^2)$.

$$\begin{aligned} \sigma_{x_s}^2 = \frac{(1-t)R^3\theta_s^2}{288}\Big(& 60t^2 - 72t^3 + 48t^4 - 77kt^2 - 12kt + 186kt^3 - 106kt^4 \\ & + 192kt^2 \ln 2 + 48kt \ln(1-t) - 72kt^2 \ln 1 - t - 384kt^3 \ln 2 \\ & + 192kt^4 \ln 2 - 12k \ln(1-t)\Big) + O(k^2). \end{aligned} \tag{22}$$

The solid line in figure 5 represents the lateral displacement σx_s for the case *A* fixed *B* free calculated for 200 MeV protons in water stopping at *B*. This result is compared with the experimental measurements which are represented as the triangles.

The lateral displacement σx_s was calculated and measured with respect to the straight line connecting *A* and *D*. This is quite an obvious choice but is not the best one can do. For any given point *D* not aligned on the pencil beam axis *AB* we can calculate a priori

the average value of the displacement of all the proton trajectories connecting A and D and use this expectation value for the calculation of the pixel address at a given depth. This curve is a straight line only for the special case $D=B$. The spatial resolution is then given by the variation of the trajectories around this curve averaged over all possible x_D values.

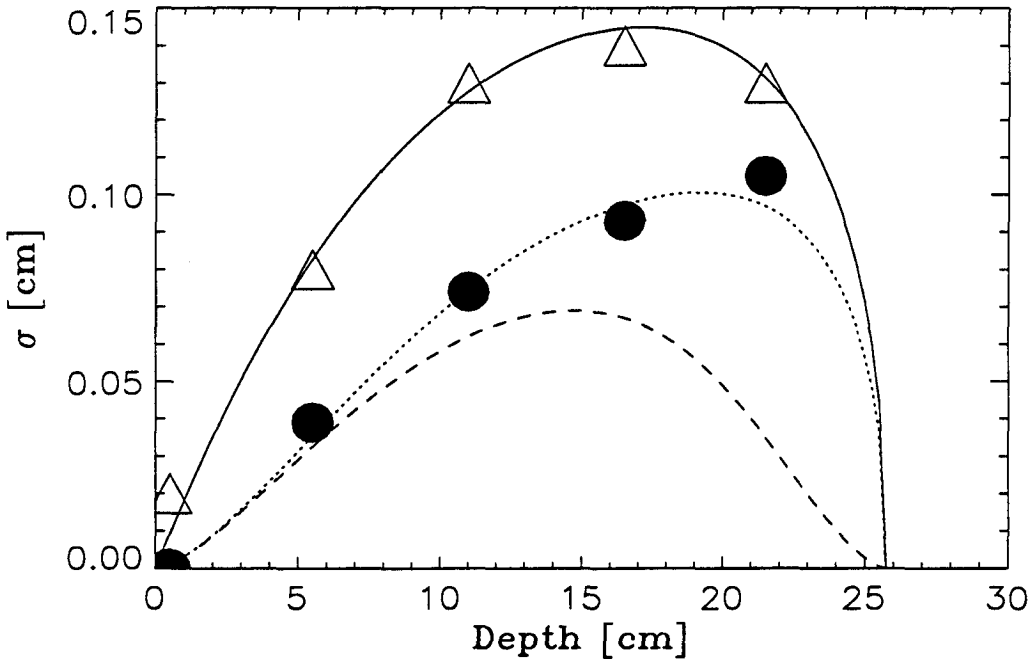

Figure 6 Spatial resolution of 200 MeV protons including energy loss as a function of depth in water. Comparison of the trajectory-case with (dashed line) and without (dotted line) angle measurement and the straight-line-case (solid line). Symbols give the experimental results.

The probability of finding protons at D which passed through A and C was calculated in the last section and given by equation (12). For the average proton trajectory we get

$$\bar{x}_{traj} = \frac{(B_o^t R(1-t)+A_o^t)D_o^t}{-A_t^1 B_o^{t\,2}+2D_o^t B_o^t R(1-t)+C_o^t A_o^t A_t^1+C_o^t D_o^t R^2(1-t)^2+A_o^t D_o^t} x_D = g_1(t)x_D \qquad (23)$$

and for the lateral displacement from this average trajectory

$$\sigma^2_{traj} = \frac{(A^t_o A^1_t + D^t_o R^2(1-t)^2)D^t_o}{2(-A^1_t B^{t\,2}_o + 2D^t_o B^t_o R(1-t) + C^t_o A^t_o A^1_t + C^t_o D^t_o R^2(1-t)^2 + D^t_o A^t_o)}, \qquad (24)$$

which is independent of x_D and is therefore already the final result (is equal to the average over all x_D). In figure 6 this result is represented as the dotted line compared to the result of section 2.3 (solid line). The corresponding measurements are shown as black circles. We obtain exactly the same result as for the case A and B fixed discussed in section 2.4, but as a more general result. We conclude that the more accurate calculation with the most likely trajectory improves the spatial resolution by about 1/3 (compared to the naive straight-line-case).

2.6 Spatial resolution with measured points and angles

In this chapter we consider again the conditions of section 2.4 but include in our calculations the assumption that the exit angle θ_D (figure 3) is measured. We consider the most probable trajectory for given measured positions x_A and x_D and angle θ_D. This gives again the pixel address for the image. The spatial resolution is then the average over all possible x_D and θ_D of the variation of the proton tracks around the most likely trajectory. The probability of finding protons at D with exit angles θ_D which passed through A and C is given by equation 11. We are interested in the width of the distribution of the x_t values as a function of fixed x_D and θ_D. Therefore we substitute in formula (11)

$$\phi = \theta_D - \theta_t \qquad (25)$$

and integrate over θ_t. We get for the average proton trajectory

$$\bar{x}_{angle} = \frac{(D^t_o + C^1_t A^t_o - B^1_t B^t_o + C^1_t B^t_o(1-t)R)x_D + (A^1_t B^t_o - B^1_t A^t_o - B^1_t B^t_o(1-t)R - (1-t)RD^t_o)\theta_D}{D^t_o + D^1_t + A^t_o C^1_t + A^1_t C^t_o - 2B^1_t C^t_o(1-t)R + C^t_o C^1_t(1-t)^2R^2 + 2C^1_t B^t_o(1-t)R - 2B^t_o B^1_t} \qquad (26)$$

$$= g_2(t)\, x_D + f(t)\, \theta_D$$

and for the lateral displacement from this trajectory

$$\sigma^2_{angle} = \frac{(A_t^1 A_o^t C_o^t - A_t^1 B_o^t - 2B_t^1 A_o^t C_o^t (1-t)R + 2B_t^1 B_o^t (1-t)R + C_t^1 C_o^t A_o^t (1-t)R - C_t^1 B_o^{t\,2} (1-t)^2 R^2 + A_o^t D_t^1)}{2(D_o^t + D_t^1 + A_t^1 C_o^t - 2B_t^1 C_o^t (1-t)R + C_t^1 C_o^t (1-t)^2 R^2 + 2C_t^1 B_o^t (1-t)R - 2B_t^1 B_o^t + A_t^1 C_0^t)}, \tag{27}$$

which is independent of x_D and θ_D and therefore is again the final result. In figure 6 this result is shown as the dashed line. The spatial resolution is improved by about 30% compared to the trajectory case given by formula (24).

2.7 Discussion

We have derived analytical formulae for calculating the spatial resolution in proton radiography, taking into account the energy loss of particles when they penetrate through matter and we compared them here with experimental results taken in our proton therapy beamline at PSI.

We discuss first the case of *A* fixed and *D* free and we restrict ourselves to a proton range equal to the sample thickness.

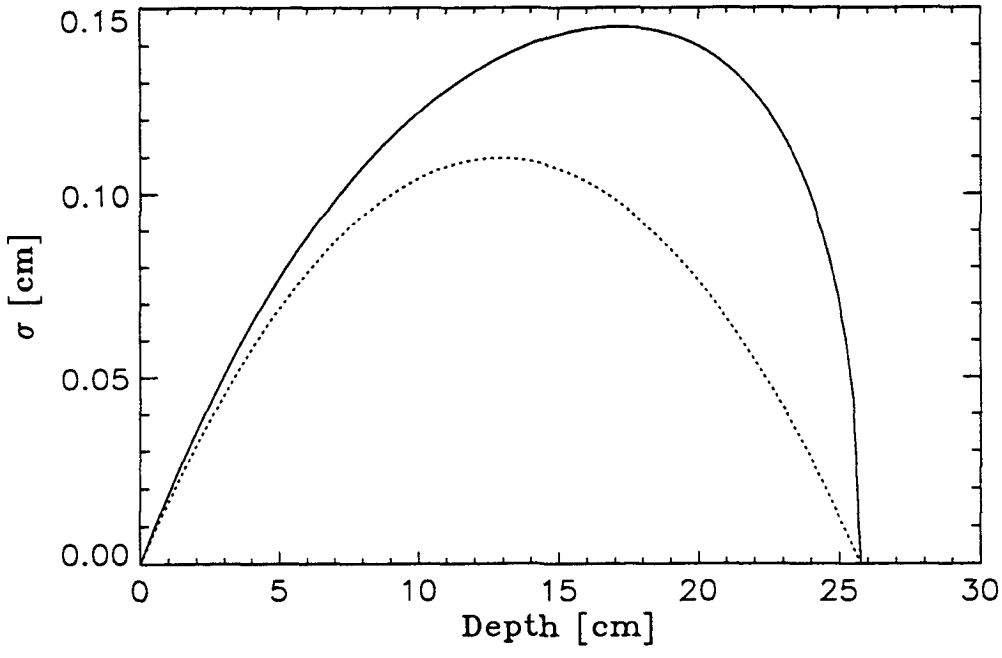

Figure 7 Spatial resolution of 200 MeV protons in water as a function of depth. Comparison of the straight-line-case with (solid line) and without (dotted line) energy loss.

Figure 7 shows the behavior of the calculated displacement in water with and without energy loss . With energy loss the maximum displacement shifts to greater depths and is no longer symmetric around $t = 1/2$. In figure 8 the maximum displacement is plotted as a function of the energy (with proton range is equal to sample thickness). We see that the spatial resolution worsens with energy loss by about 25% at all energies.

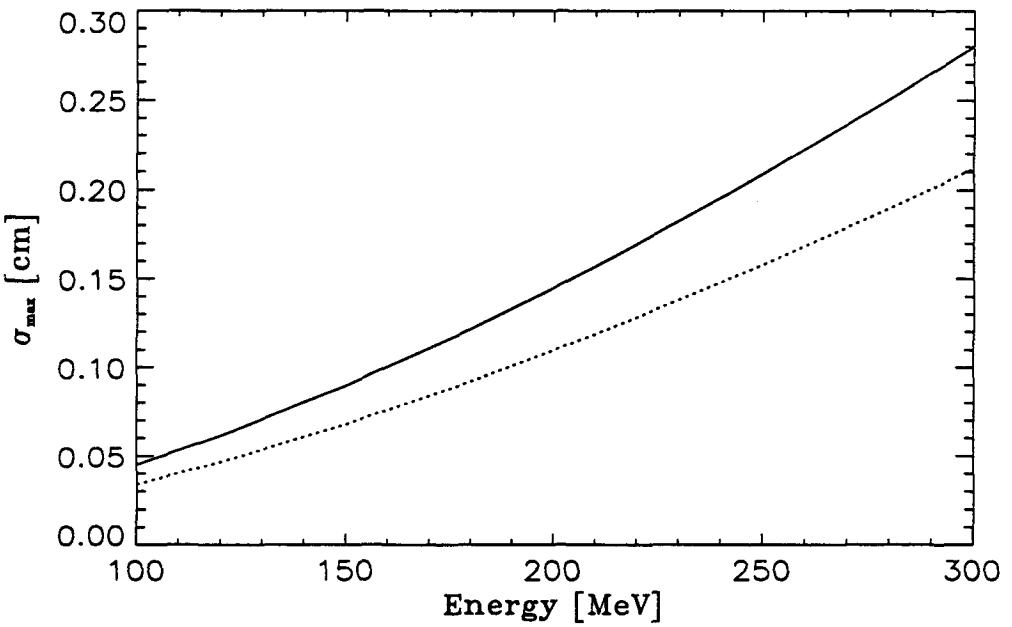

Figure 8 Maximum value of the spatial resolution as a function of the initial energy of protons in water calculated with the straight-line-case with (solid line) and without (dottedline) energy loss for a sample thickness which is equal the range.

The assumption that range is equal sample-thickness represents the worse case for the spatial resolution. Figure 9 shows the behavior of the spatial resolution as a function of energy with fixed sample thickness (25.75 cm) as the solid line. The dotted line represents the behavior as a function of energy of the density resolution due to range straggling (Appendix A). The spatial resolution increases by about 30% as the energy varies from 200 MeV to 300 MeV, but the density resolution worsens by about a factor of 2.

We can now compare the different techniques of measuring the proton coordinates. We discuss first the double-collimator-case (A and B fixed). This method has the advantage of providing the optimal spatial resolution, permits, in principle, fast data taking since one can measure the beam intensity attenuation without the need to detect single events, but requires on the other hand the mechanical scanning of the exit collimator. The main disadvantage is given by the unnecessary dose given to the patient, deposited by the protons which are lost in the exit-collimator and which do not contribute to the radiographic image. For a 200 MeV proton beam the extra dose factor can be estimated

to be 14 and 7 for 1mm and 2mm wide collimators, respectively. Another advantage of this method is that there is no mixing of density information in the reconstructed images, since the *AB*-fixed-image is focused at all depth simultaneously.

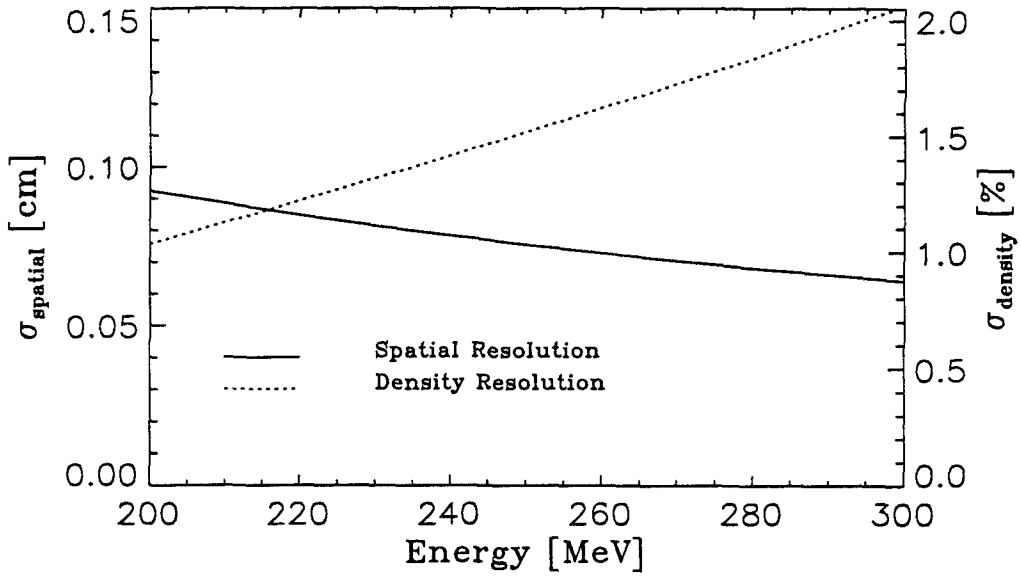

Figure 9 Variation of spatial and density resolution for protons with different initial energies in a homogenous water bath of thickness 25.75 cm.

The same spatial resolution can be achieved by measuring the entrance and exit coordinates with MWPCs, provided that the pixel addresses are calculated on the base of the most likely trajectory given by equation (24). With this method the information of all protons is used achieving minimum dose burden to the patient. Another advantage is that this method can be used with broad parallel beams and slow coarse beam scanning. The disadvantage of this technique is given by the necessity to measure single events in coincidence, which could become a limiting factor (speed of data taking) for the practical acquisition of the images.

The same reasoning can be applied to the case where the exit angle is measured as well. Silicon detectors with their excellent spatial resolution are probably more indicated than MWPCs for this application, since they provide very good angular resolution without requiring a large distance between detectors on the exit side of the phantom.

Another possibility to improve the spatial resolution of proton radiographs was suggested by Martin[14]. His method is based on the "measurement" of the entrance coordi-

[14] R.L. Martin, *Private Communication* (1993)

nate only (*A* defined by the position of the scanned pencil beam). On the exit side only the energy (or range) is measured. The spatial resolution is then improved by taking two opposed images. Details in the first half of the patient would be resolved by the conventional beam direction, with details in the second half of the patient being resolved by use of the opposite beam direction. The advantage of this method is the fast data taking speed (beam intensity measurement) but it requires a fast beam scanning of a very tiny collimated pencil proton beam.

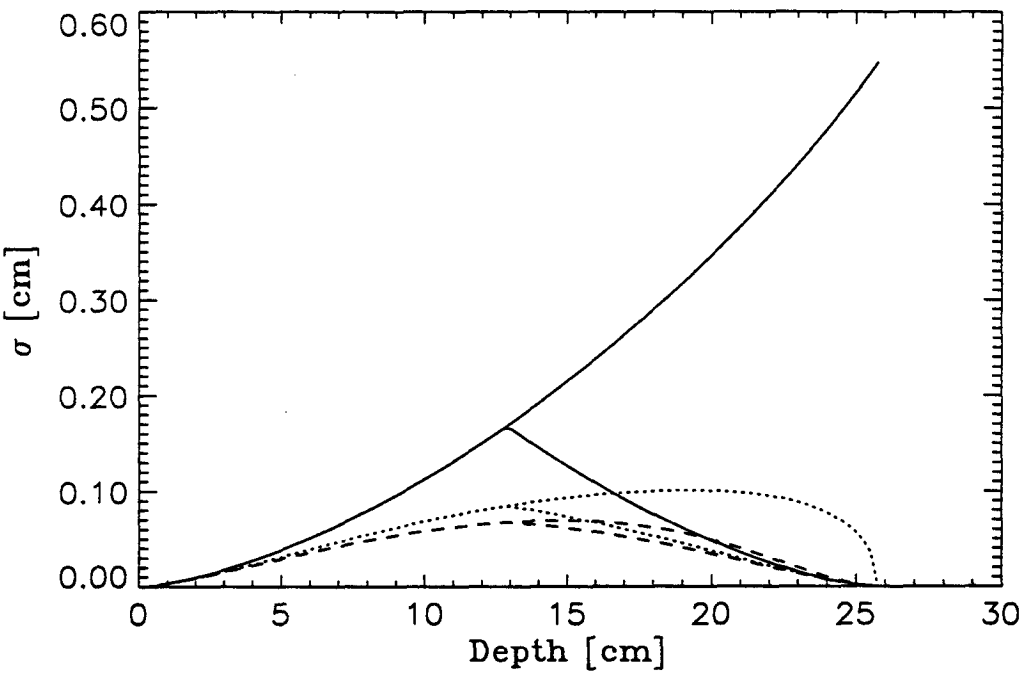

Figure 10 Spatial resolution of 200 MeV protons in water including energy loss. Comparison of the one-coordinate-measurement (solid line), and the trajectory case with (dashed line) and without (dotted line) angle measurement together with the resolution resulting from two "opposed" images for each of the three techniques.

The results of the calculations for 200 MeV protons in water are shown for comparison in figure 10 for the different techniques discussed (the *AB*-fixed-method and the average-trajectory-method are giving the same spatial resolution and are therefore plotted as a single case). The solid line represents the spatial resolution for the case of the measurement of the entrance coordinate alone and the dotted line for the average-trajectory-case with entrance and exit coordinates measurements. The dashed line shows the case of measured positions and angles. By measuring twice the position of the protons along its trajectory the position resolution is improved up to a factor of 5.5 depending on depth. By measuring all proton parameters at entrance and exit of the phantom the factor is increasing to 8.0. If two parallel opposed images are taken with

the different techniques the spatial resolution of the average-trajectory-case is better but only by a factor of 2.0 without and 2.5 with angle measurement.

The average-trajectory-case always gives the best spatial resolution while achieving very low dose to the patient, but requires single event data taking. For patient positioning for proton therapy this could be a realistic approach to produce images with very low dose. Only a few protons per pixel are needed to provide the range information with the precision relevant for therapy. For diagnostic images of high density resolution with high proton statistics the time for getting the images could become a severe practical limitation. In this case the single-coordinate-method is probably preferable even at the expenses of a reduced spatial resolution.

3. Proton Radiography as a Tool for Quality Control in Proton Therapy

3.1 Introduction

The more precise a radiation therapy treatment is, the more important is the quality control of patient treatments. A first important task is to check the correct positioning of the patient with respect to the beam. As the calculated proton dose distribution is based on the predicted range of protons in the patient, another requirement is the verification of the range and range variations of the protons in vivo in the patient. Proton radiography can fulfil these requirements simultaneously. For this purpose we produced proton radiographies of an Alderson phantom and of a sheep's head. We measured the residual energy of protons which traversed the different phantoms and calculated the range of each particle. The images were produced by plotting both the range information and range uncertainty information as a function of the proton position and were compared to the predicted results of the treatment planning algorithm.

Sources of range errors include: uncertainties in the computer tomographic (CT) data, which are the basis for the treatment planning program, and errors occurring in the treatment planning software (Alpen et al. 1985, Chen et al. 1979). Range variations due to inhomogeneous interfaces parallel to the beam are also very difficult to predict by the treatment planning software. Such uncertainties in range can result in an overdosage of critical tissue and target misses. In this section we show that proton radiography can help to solve, or at least to provide a better understanding of these problems.

Proton radiography and tomography for diagnostic purposes was investigated in the 1970's (Hanson et al. 1981, Hanson et al. 1982, Mofett et al. 1975, Koehler and Steward 1973ab). The motivation for these projects was to obtain images of low contrast lesions in human specimens that were superior to conventional x-ray techniques. In addition, these authors where encouraged by the dose advantage of proton radiography over x-rays. But due to the success of x-ray computed tomography the interest in proton tomography vanished. In the context of the proton therapy project at PSI we have decided to re-investigate proton radiography from the point of view of its potential as a quality control tool and to provide the capability of proton radiography in the design of the proton therapy facility. The PSI proton gantry is equipped with movable devices which can be shifted in front of and behind the patient and which should contain the equipment for proton radiography. The beam transport system has been designed to provide energies up to 270 MeV, which is high enough for the penetration of protons through the patient's body (Pedroni et al. 1994).

3.2 Experimental apparatus

The experimental apparatus depicted in figure 11 was placed in the beam line dedicated to proton therapy at PSI. The 590 MeV proton beam was degraded to 219 MeV, corre-

sponding to a range of 30.5 cm in water, and was analysed in momentum and phase space in the beam line following the degrader (Pedroni and Enge 1993). The beam used had a spot 19 mm (FWHM) wide by 18 mm (FWHM) high. The beam was restricted to a 0.6 % (FWHM) momentum band in order not to affect the width of the detected residual energy distribution. The horizontal and vertical beam divergence was about 15 mrad (FWHM).

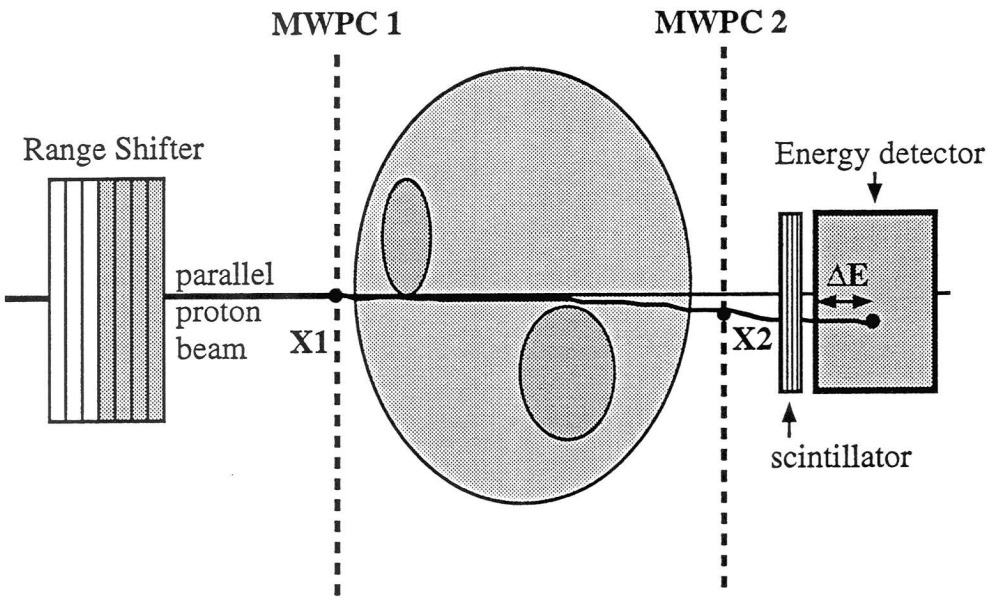

Figure 11 Experimental apparatus. The proton beam was varied in energy with the range shifter. For each proton the entrance and exit coordinates, when entering and leaving the phantom, were measured with two multi wire proportional chambers (MWPC) and its residual energy was measured in a NaI-crystal. A plastic scintillator was used to trigger the event.

Protons were first detected in front of the phantom in a position sensitive multiwire proportional chamber (MWPC 1) with a wire spacing of 2 mm. After penetrating through the phantom each proton was detected 25 cm behind the first chamber in a second one (MWPC 2), then in a scintillation counter and finally in a NaI detector where it was stopped. The images were produced by scanning the sample in both directions transverse to the beam. The phantom position was controlled by computer, using servo-mechanism units, one for the horizontal and one for the vertical translation. The signal from the scintillation counter was taken in coincidence with the signal from the range shifter, the phantom scanner, the two multiwire chambers and the NaI detector to form an event for the data taking system. Data taking was accomplished by means of standard CAMAC modules read-out by a Starburst computer. The data taking permitted an

average rate of 1000 protons per second, which resulted in a typical exposure time of roughly 2 hours. The Starburst transferred unprocessed event data to a VAXstation.

In the analysis carried out on the VAXstation, the spatial information of the two wire chambers was used to reconstruct the intercepts of the most likely proton trajectory of every event in equally spaced parallel planes between MWPC 1 and MWPC 2. The most likely proton trajectory was calculated to be the most probable proton path between two points through which the proton passed. The computation was done according to the method described in section 2 (see also Appendix C). Only events for which one wire of each chamber fired were considered for the analysis. To exclude protons scattered through large angles we chose the maximum difference between the chamber coordinates to be less than 2 cm in both directions transverse to the beam. The intercept coordinates of the calculated proton trajectory and the plane to be reconstructed were used to form images at different depths in the phantom in order to better resolve structures located there.

The protons were stopped in a NaI detector which measured their residual energy. The crystal had a diameter of 7.5 cm and a thickness of 10 cm, sufficient to completely stop the protons. The energy resolution was measured for ^{60}Co γ-rays to be 95 keV (FWHM). The NaI output was amplified and digitised using a LeCroy analogue-to-digital converter (ADC). Only protons which impinged on the central region of the NaI crystal were detected, eliminating edge effects. In addition the proton energy was calibrated as a function of the entrance point on the crystal.

The proton ranges were varied with a range shifter consisting of 40 polyethylene plates which can be moved singly into the beam path. The range of the protons was reduced with each plate by 0.47 cm. The number of plates required to reduce the range of the protons was adjusted on-line as a function of the measured density for each phantom position and moved under computer control into the beam.

We scanned with our apparatus the head of the Alderson phantom which was fixed in a water phantom with 0.5 cm Lucite walls and enclosed in a plastic foil. The scans were done both with the water filled phantom or without water with the proton range adjusted with the use of the range shifter. In addition we scanned a sheep's head to have measurements of real biological tissue. The sheep's head was cut from the body and fastened in an aluminium box. The box was filled with moulage material which had water equivalent properties (Perret 1982). CT-scans, using a GE Scanner 9000 were made of the Alderson phantom, with and without water, with a slice thickness of 2 mm as well as scans of the sheep's head using both 5 mm and 2 mm slice thicknesses. The moulage material of known stopping power and Hounsfield values was subtracted from the images leaving the information of the biological material only. In all measurements a reference Teflon sample was scanned.

3.3 Basic properties of proton radiography

3.3.1 Multiple Coulomb scattering and spatial resolution

Of considerable importance for radiography are the small angle deflections of protons due to their interaction with the Coulomb field of the nuclei of the traversed material. The cumulative effect of these random deflections can be modelled to a first approximation by a Gaussian angular distribution. This multiple Coulomb scattering produces uncertainties in the proton trajectories, governs the spatial resolution of proton radiography and is therefore the limiting factor for the utilisation of proton radiography as a diagnostic tool. A detailed discussion of the spatial resolution of proton radiography is given in section 2. We concluded there that a spatial resolution of 1 mm can be achieved by measuring the coordinates of the entrance and exit points for each proton. The resultant resolution is poorer than that of x-ray images, but is good enough for quality control purposes in proton therapy. As proton radiography is to be used primarily as a quality assurance tool, no improvement in spatial resolution is required, since the underlying physics of proton therapy is essentially the same as for radiography.

3.3.2 Energy loss and density resolution

The attenuation of a beam of monochromatic protons passing through homogeneous matter is small until the protons are near the end of their range. The dotted line in figure 12 shows the flux curve for protons, neglecting nuclear interactions, which demonstrates the steep negative slope that is found in the last portion of the proton range.

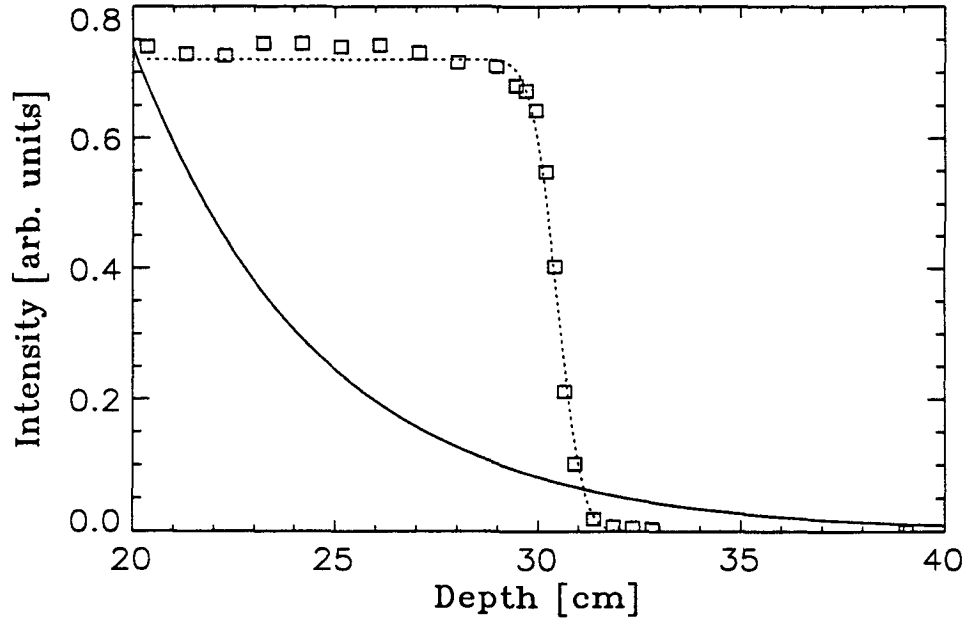

Figure 12 Flux of 219 MeV protons (dotted line) and 50 keV photon (solid line) passing through water. The symbols represent measurements.

Thus a small change in the thickness of the absorber will result in a large change in the number of particles which pass through it. The steepness of that slope is given by the range straggling of protons passing through the matter and is characterised by the sensitivity of the range measurement. The range measurement of each individual proton can either be done by direct range measurement with, for example, a range telescope or with an energy measurement where the measured energies have to be transformed into proton ranges. Whether range detection or energy detection is the better choice depends on the sensitivity of the detector. For comparison, in figure 12, the transmission of x-rays is shown, where the flux is attenuated in a near-exponential fashion with increasing depth in the absorber.

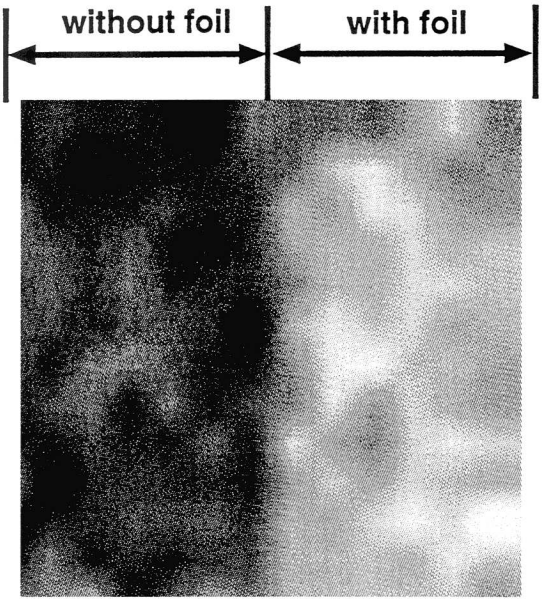

Figure 13 Proton radiography of a plastic sheet (thickness ~ 0.3 mm) fixed on a homogeneous water phantom.

With the experimental apparatus described in section 3.2 we expect to be able to detect variations in integral density as small as 0.1 % with a low dose to the patient. Figure 13 shows the image of a homogeneous water phantom with a sheet of thin plastic which was fixed over the right hand side of the water tank. The difference in integral density of the water phantom and the water phantom and foil was about 0.1 %. Thus, with the same dose applied to the patient one can detect changes in effective absorber thickness that are considerably smaller than those observable with other radiographic techniques. Such a density resolution is the result of the characteristic loss of energy of protons passing through matter. For protons with energies of the order of 200 MeV, loss of kinetic energy results from ionisation of atoms in the matter. This energy loss per centi-

metre, called the stopping power, per proton can be calculated from the well known Bethe-Bloch equation (28).

$$\frac{dE}{dx} = K\frac{(\rho N_g)}{\beta^2}\left\{\ln\frac{2m_e c^2\beta^2}{I\left(1-\beta^2\right)} - \beta^2\right\} \qquad (28)$$

where K is a constant, βc is the velocity of the proton, I is the mean ionisation energy of the target atoms, m_e is the mass of the electron and we have omitted unnecessary correction terms.

The energy loss of protons is thus mainly dependent on the electron density (ρN_g) of the traversed matter and on the ionisation potential. For most materials in humans, Z/A is relatively constant which means that the stopping power is proportional to the physical density ρ, in contrast to the mass absorption coefficient for x-rays, which varies in a complicated manner with Z and A (Appendix B).

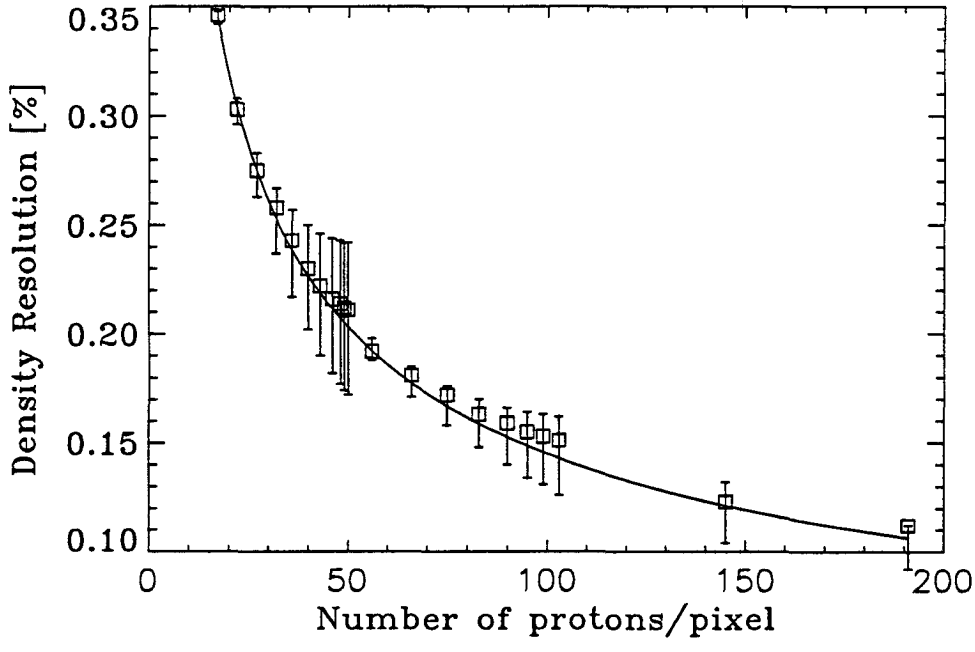

Figure 14 Plot of the density resolution as a function of the number of detected particles per pixel. The symbols represent measurements of the resolution in a homogeneous water phantom with different statistics. The solid line is the calculated prediction.

It is a further characteristic of protons that they lose kinetic energy in discrete steps by interaction with atomic electrons. As this process is statistically determined, a monoenergetic beam of protons shows an energy spread after passing through a homogeneous medium. For 219 MeV protons passing through biological material, the standard devia-

tion of this statistical process, expressed as a percentage of the mean range, is approximately 1.1. This factor determines the inherent physical limit for the density resolution of one detected proton. The density resolution increases with the number of detected protons per pixel according to the usual statistical laws. Figure 14 shows the density resolution as a function of the number of detected protons per pixel. The data were produced by taking images from a homogeneous water bath with different proton statistics. The solid line comes from calculation (including our detector energy resolution); the squares represent experimental results.

3.3.3 Energy deposition and dose to the patient

The stopping power increase as the particle slows down gives rise to the Bragg peak as is shown in figure 1. The largest amount of proton energy is deposited at the end of its range. Since for proton radiography the proton is stopped in the detection system (see figure 19) most of the dose is deposited there and not in the patient. The applied dose for a proton image of 26 cm by 14 cm size obtained with roughly one million events was calculated to be 0.01 mGy. A x-ray radiograph with both the same spatial- and density resolution would result in a 10 to 20 times higher dose.

3.4 Calibration and stability of the apparatus

The NaI detector response was calibrated with the range shifter and a 16.4 cm thick Lucite block fixed between the two multiwire chambers. Different numbers of range shifter plates were put into the beam and Gaussian fits were made to the corresponding ADC-spectra. A linear energy response of the detector was assumed. The energy calibration of the ADC signal was obtained by linearly fitting the data as a function of the energy, calculated from the total amount of material in the beam path using range-energy tables (Bichsel 1972, Janni 1982). The corresponding calibration curve for the transformation of ADC-channels into water equivalent range was gained from the fit parameters and from the range-energy look-up table. This is shown in figure 15.

The NaI measuring system covers a domain of proton ranges between 11 cm and 30 cm. Using the range shifter, this can be extended from 0 cm to 30 cm for 219 MeV protons. For this reason, it is not necessary for the samples to be scanned in water. Es-

pecially when using a radiographic system with patients, a large dynamic range is required for scanning the patients without a water bath.

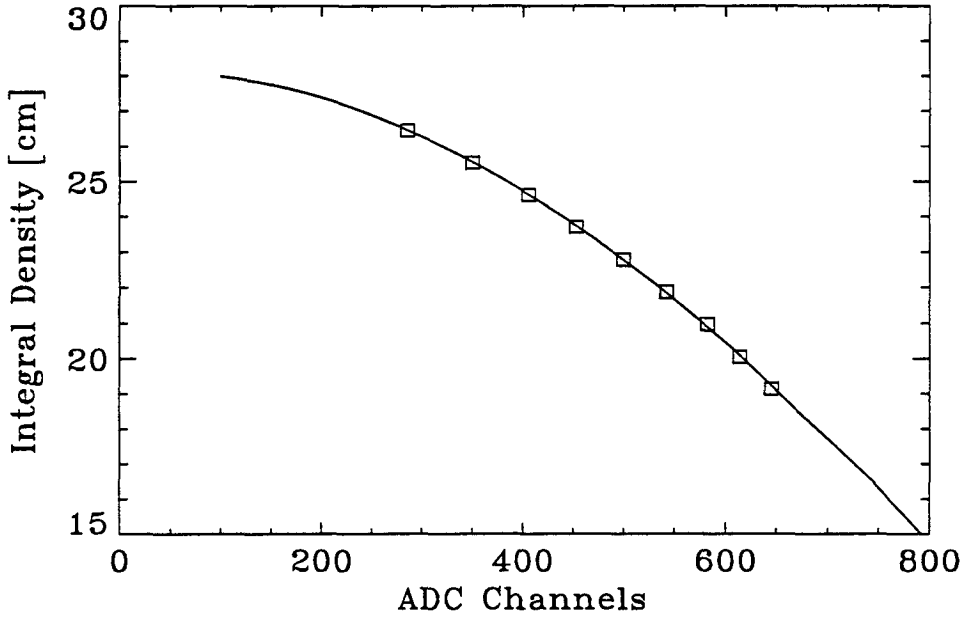

Figure 15 Calibration curve for the transformation of ADC-channels into water equivalent range. The symbols represent the data points for different number of range shifter plates.

The density information contained in proton radiographs is derived from the measurement of the residual energy of the protons leaving the sample. The density resolution is therefore directly related to the energy resolution of the measuring system, including the detector resolution, the energy band of the beam and the effects of energy straggling. From a comparison of the measurements with the simple model discussed in Appendix A the following contributions to the resolution for the different components as a percentage of the mean range can be calculated.

1. Range straggling: 1.1 %
2. Density resolution of the detecting system: 0.5 %
3. Momentum band of the beam: 0.4 %.

These have all been calculated for 219 MeV protons passing through a 23 cm water sample. Thus the total rms range error for a single proton event is around 1.3 %. The stability of the NaI measurements of proton residual range has been investigated during a scan of the sheep's head. During each horizontal scan the proton beam passed through homogeneous moulage material of known thickness (23.1 cm water equivalent thickness). In this regions the water equivalent range of the protons was measured repeatedly. These range measurements are plotted as a function of time in figure 16. It can be seen that the RMS deviation of the mean value of the range for this 2 h and 25 minutes

scan is 0.13 %. This includes unknown inhomogeneities in the density of the moulage material.

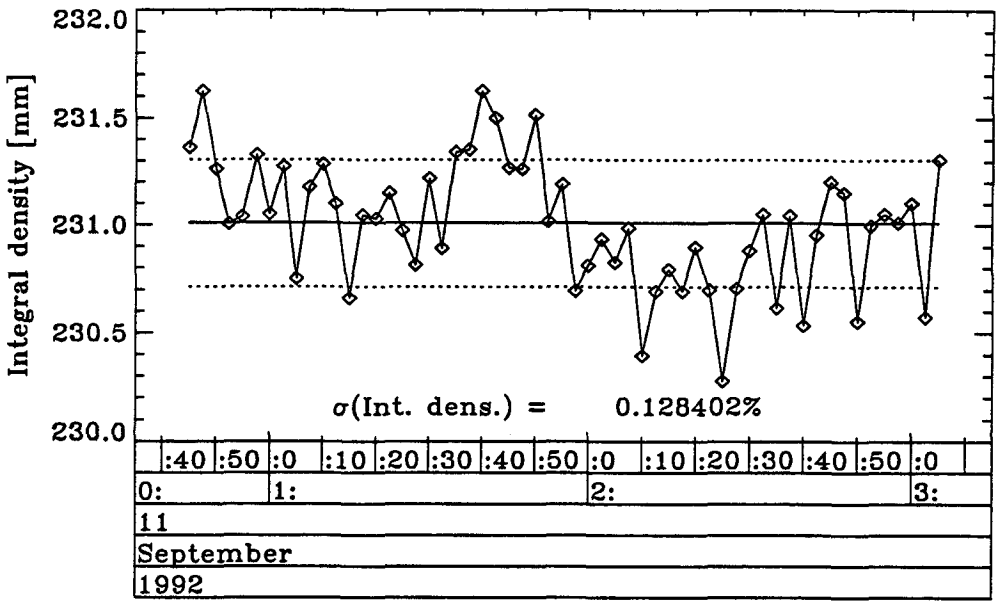

Figure 16 Stability of the measurement of the integral density. The symbols represent repeated measurements of the water equivalent range of homogeneous moulage material of constant thickness as a function of time. The standard deviation of the measurements is 0.13 % of the whole range.

3.5 Verification of the patient positioning

Inaccurate positioning of the patient can result in the damage of critical structures or missing of the target. The usual way to check the patient positioning before irradiation is to provide x-ray radiographies of the patient in the treatment position and to compare these images with digital radiographies reconstructed (DRR's) from the CT data used for treatment planing.

Another possibility is to take proton radiographies directly on the proton gantry. The description of the mechanical mounting of the proton radiography devices on the gantry is given elsewhere (Pedroni et al. 1994). The expected advantage is that the images can be taken exactly under the same geometrical conditions as for the treatment. Hence, the

images are true proton-beam's-eye-view projections, as opposed to x-ray images which are conical projections from a given point source.

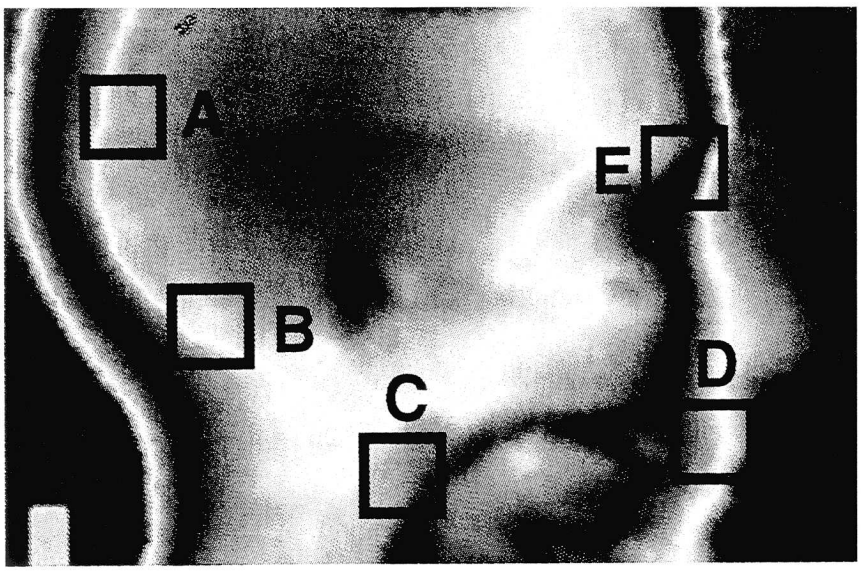

Figure 17 Proton radiography of the Alderson phantom using 219 MeV protons and the range shifter. The five marked regions were used to determine the precision of matching a proton image with a DRR.

To verify the accuracy of proton therapy, a proton radiography of the Alderson phantom was taken for position verification and this is shown in figure 17 with five regions of the image marked. The corresponding DRR was calculated using the CT information, was matched to the proton image and the correlation between the two images for the selected regions as a function of their displacement was calculated with

$$R_{uv} = \frac{\sum_j \sum_i D_{ij} P_{ij}}{\left\{ \sum_j \sum_i D_{ij}^2 \right\}^{\frac{1}{2}}} . \qquad (29)$$

D_{ij} and P_{ij} are the voxel values of the overlapping region of the DRR and the proton radiography respectively and R_{uv} is the correlation for a horizontal and a vertical shift u and v respectively. Figure 18 shows for the five regions the correlation plotted as a function of the relative voxel number in the horizontal direction. It can be seen that the

correlation shows its maximum when the relative voxel number is equal to zero corresponding to correct positioning of the patient.

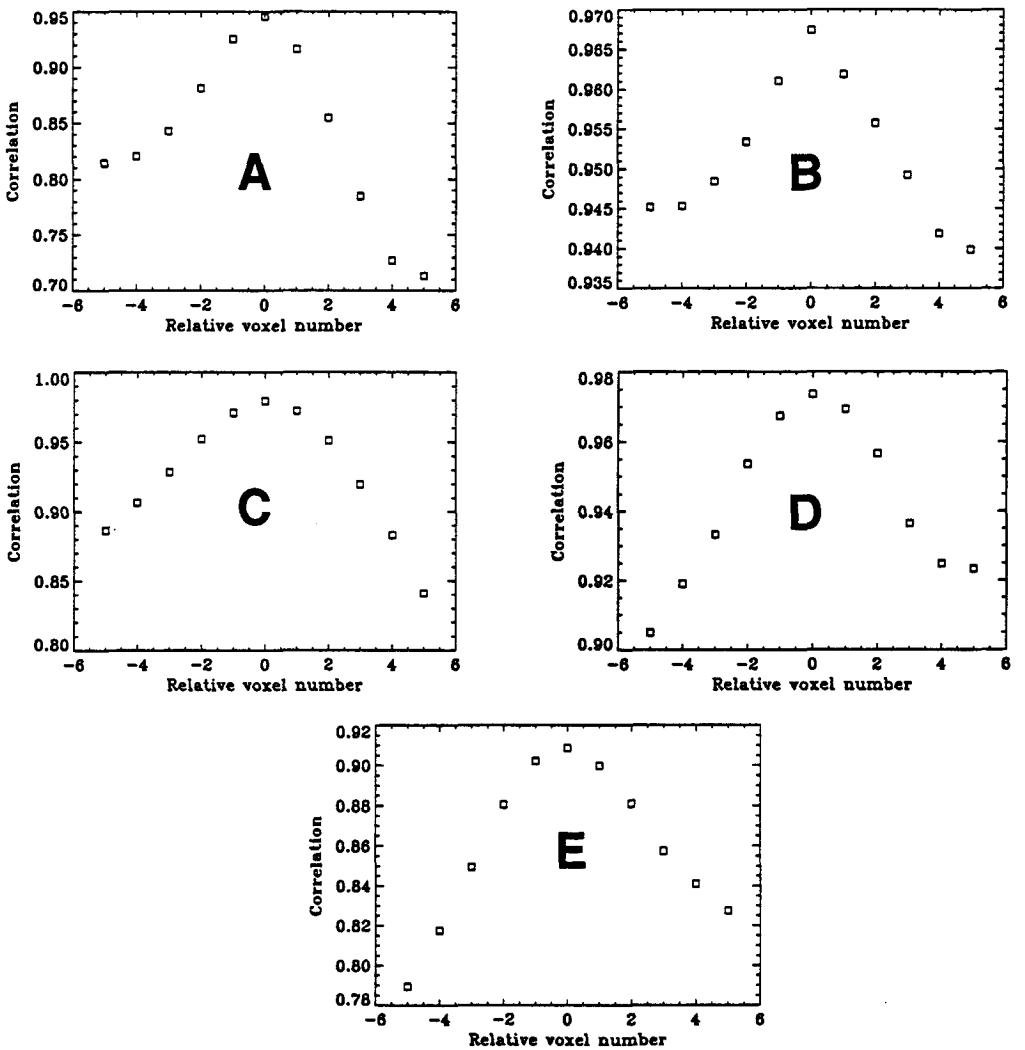

Figure 18 Correlation between calculated DRR and proton radiography as a function of the shift between the two images measured in voxel units for the 5 selected regions shown in figure 17.

The voxel size of the proton image and the DRR was 2 mm, i.e. the position check provided by proton radiographic images is better than 2 mm. We conclude that proton radiography is an adequate tool for verifying the position of the patient in proton therapy.

3.6 Range uncertainties

Effects due to density inhomogeneities in the traversed material can influence the range of protons. Neglecting them may result in a low dose being delivered to parts of the target volume or an unintentional dose to critical structures distal to the target volume.

How the combined effect of multiple Coulomb scattering and density inhomogeneities can influence the range of protons and their measurement with the proton radiographic equipment is sketched in figure 19.

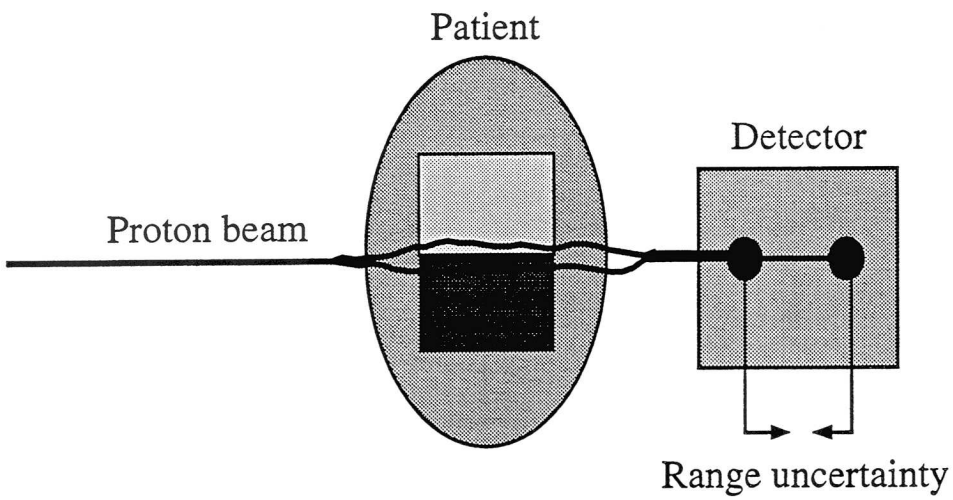

Figure 19 The range of protons entering and leaving the patient at the same longitudinal coordinate can be different due to inhomogeneity interfaces transverse to the beam.

A proton which passes close to an interface between a low density and a high density tissue region in the patient can take, with a certain probability, either the path through the low density material or through the high density material due to multiple Coulomb scattering. In the absence of multiple Coulomb scattering, the inhomogeneities would simply shift the range of protons by a distance equal to the integrated density along its path. However, the effect of multiple Coulomb scattering leads protons which enter and leave the sample through the same entrance and exit points, to follow different trajectories and thus to cause range uncertainties. Similar range uncertainties are present also for therapy and can produce significant errors in the dose distribution. Proton radiographs detect the range variations for the whole body and may be used as a warning to change the direction of the field to be irradiated or for the determination of safety margins around the tumour volume.

Urie et al. (1986) measured the shape of the Bragg peak of 160 MeV protons that had passed through geometrical phantoms and behind bony structures of a water filled skull

in order to study the degradation of the Bragg peak due to inhomogeneities. In addition they used heavy ion beams (carbon and neon) to obtain the shape of the Bragg peak behind the head and the abdomen of a patient. Their results show a broadening of the distal fall-off (90 % to 20 % dose) of a modulated proton beam from 6 mm to over 32 mm. The heavy ions show similar behaviour. The neon Bragg peak was degraded at the base of the skull from 3 mm to 15 mm and the carbon Bragg peak showed a broadening in regions of the gastrointestinal tract from 12 mm to 32 mm.

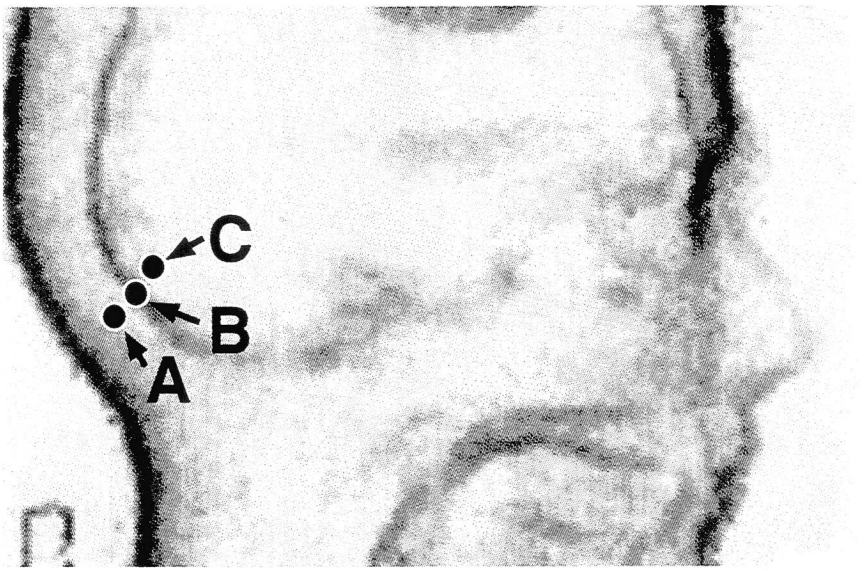

Figure 20 Proton image created using the information of the width of the range spectra in each pixel. Dark regions indicate critical situations where the proton ranges are spread.

Here we report on studies of the 219 MeV proton beam in both tissue specimens and an Alderson phantom. Proton radiographs created with the standard deviation σ of the range spectra were taken to study quantitatively the range variations of protons traversing inhomogeneities. The proton images were reconstructed in the middle plane halfway between MWPC1 and MWPC2. In figure 20 a "σ"-image of the Alderson phantom is shown. The dark regions represent regions of broad range spectra. The three points A, B and C indicate the transition of a bone structure to muscle tissue.

Figures 21 shows the corresponding range spectra at these points. Points A and C show well defined tissues like muscle and bone structure respectively. The spectra have a width of around 4.5 mm which is the expected width due to range straggling and taking into account the initial momentum band. However the spectrum measured in point B, which is at the interface of these two tissues, broadens to around 20 mm. It should be noted that the range spectra were obtained from protons traversing the whole head whereas in a treatment situation, one is interested in the range variation caused by pro-

tons stopping in the head. Hence our measurements give an upper limit for the range error which can occur during treatment.

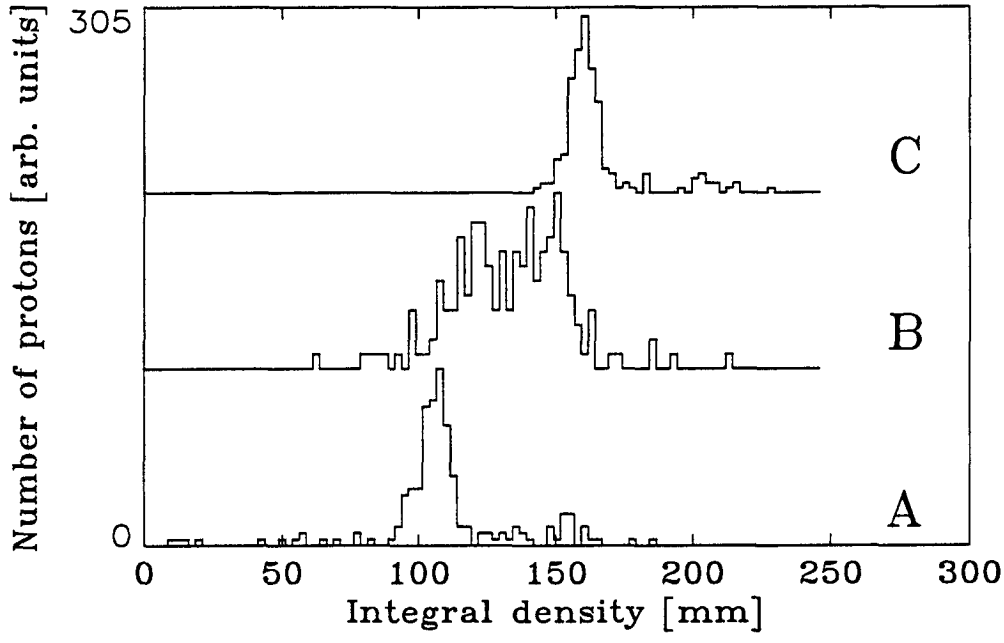

Figure 21 Range spectra for the three selected locations A, B and C labeled in figure 20. Regions A and B belong to pixels where the protons passed more or less homogeneous material. Region C represents a pixel where the protons traversed inhomogeneity interfaces parallel to the beam.

To identify those regions which cause broad range spectra and therefore dose errors figure 30 shows, as a gray-scale image, the DRR of the Alderson phantom head. The colours (red: > 15 mm, 15 mm > blue > 10 mm, 10 mm > yellow > 5 mm) in the images indicate the standard deviation of the range spectra. From the colours, we can distinguish those regions with additional straggling caused by inhomogeneities. As can be seen, range uncertainties of over 15 mm occur in regions where the protons passed close to tissue characterised by a strong density gradient orthogonal to the beam. Critical situations in the Alderson head are labelled in figure 22. In the region around point A the critical structures are tissue interfaces between the oral cavity and the mandible ramus (maximum variation = 25.6 mm, mean variation = 17.4 mm), B labels directions where mastoid air cells and the sigmoid sinus (22.2 mm, 16.7 mm) are in the beam path, C marks beam incidence with the frontal sinus (22.0 mm, 15.7 mm), D labels regions where the proton beam passed tangential to the skull (19.0 mm, 12.0 mm), E describes areas where protons traversed mastoid air cells and bone brain interfaces (18.5 mm, 15.3 mm), F marks the beam direction where the protons traversed the sphenoid sinus (18.2 mm, 12.5 mm) and G the maxillary sinus and the ethmoid air cells (16.8 mm, 13.3 mm). Such range variation measurements could be used as an estimate for the

necessary safety margins around the target volume, especially if the tumour is located behind such critical regions where big range variations can occur.

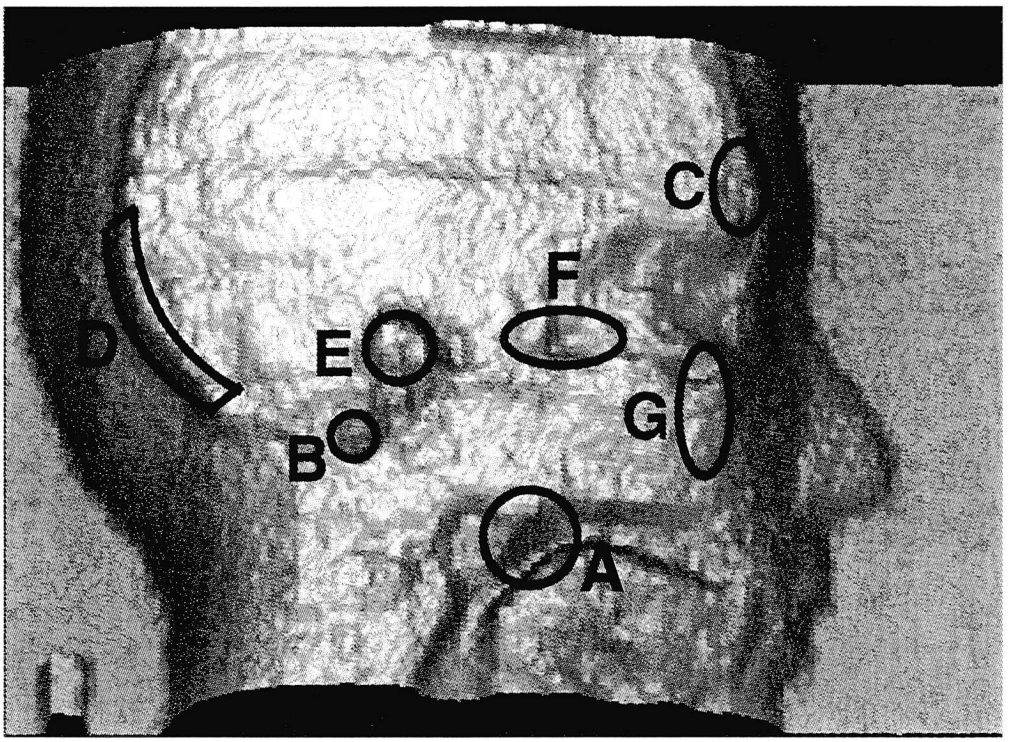

Figure 22 Radiography produced with the mean ranges of the proton spectra in each pixel. The selected regions label situations where big range variations can occur

Range variations can influence the dose distribution for proton treatments and proton radiography can be used for measuring these uncertainties and may help to find optimal beam directions.

Another way to get information on range uncertainties is to perform Monte Carlo simulations of the therapy dose distribution and the proton radiography in the region of the patient to be treated. Experimentally obtained proton radiographies may be used to verify the Monte Carlo calculations of proton radiographies and to give more confidence in the results obtained for therapy conditions. At PSI a Monte Carlo Code is being developed (Tourovsky et al. 1993), used to simulate proton radiographies and dose distributions for therapy.

3.7 CT-Calibration and range measurement

3.7.1 The calibration of the CT data

Computer tomographic (CT) images of a patient represent the basic information for the proton therapy treatment planning program. CT data are used to define the position of the target volume and of the critical structures and to quantify the inhomogeneities which are in the path of the proton beam. The CT-images are taken with photon beams and are therefore images of photon attenuation data. The proton therapy treatment planning software calculates the dose distribution on the basis of a range calculation for the protons and therefore needs data which can be used to describe the interaction of the proton beam with the patient's tissue. The photon attenuation coefficients of the CT data have therefore to be converted into a water equivalent path length, the so called relative stopping power, in order to provide the residual range for the proton beam. This transformation is usually done by direct measurement of both the water equivalent path length and the photon attenuation of different tissue substitutes (Chen et al. 1979, Moyers et al. 1993) or by calculation (Mustafa and Jackson 1983). The relation between stopping power and Hounsfield values is not unique. Due to the different chemical composition of tissues, it is in principle possible to have different relative stopping powers for the same Hounsfield value. This raises the question on how well one can predict ranges using calibrated CT data in practice.

We measured the stopping power of tissue substitutes with our radiographic system. The radiographic range measurement was done with the different samples immersed in a 23 cm water bath. For the bone substitute HB/SR4 we calculated the relative stopping power. In addition, the tissue substitutes were scanned in a GE 9000 scanner at 120 kVp to obtain the Hounsfield values. In table 4 the measurements of the relative stopping power and the Hounsfield values are listed together with model calculations for real tissues (see Appendix B). In figure 23 the derived calibration curve is shown as the solid line with the data points for the tissue substitutes (squares). The tissues with Hounsfield numbers up to water are assumed to be a mixture of water with air. For Hounsfield values greater than 1000 the tissue is assumed to be a mixture of bone mineral and water (Chen et al. 1979).

All these approximations do not describe real situations well enough to be used for a precise proton treatment. The first error to be considered is the precision of the CT data itself. Errors of the measured Hounsfield values of the order of 1.5 % and of their position dependence of 3 % (Moyers et al. 1993) give rise to errors in the predicted proton ranges. Moreover one can find cupping artefacts in CT data close to high-low density interfaces. This effect manifests itself by a decrease of Hounsfield values extending several pixels into high density tissue with a corresponding increase in the regions of low density. Range calculations of beams parallel to this interface are correspondingly

affected. It must also be remembered that the tissue substitutes are not real tissue, with the oxygen often being replaced by carbon in such compounds.

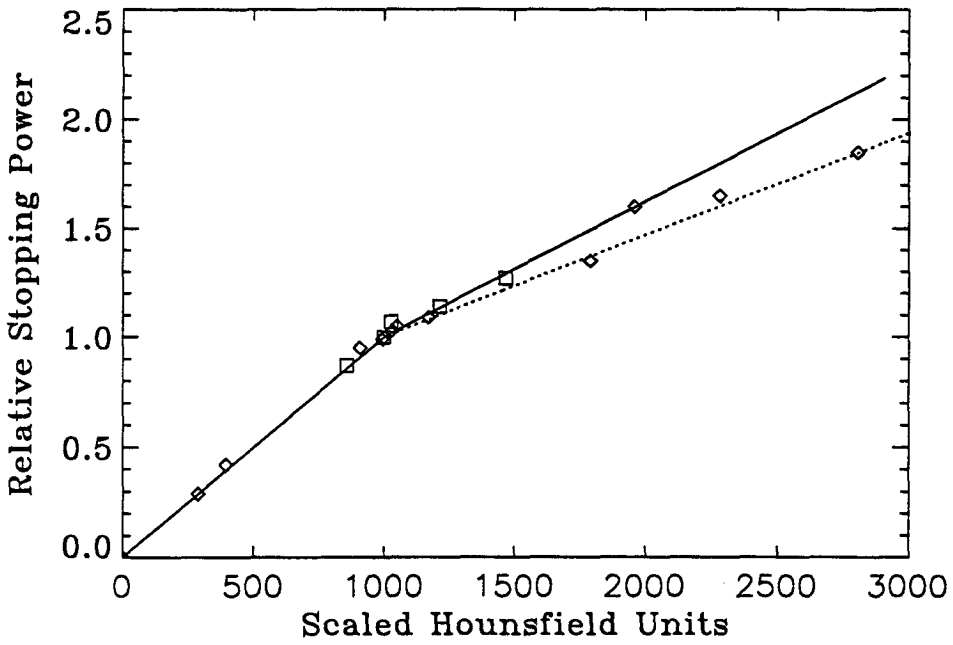

Figure 23 Calibration curves for the transformation of Hounsfield values into relative proton stopping power. The solid line shows the tissue-substitute-calibration, the dashed line the stoichiometric-calibration for biological tissues. The squares represent results of the tissue substitute measurements and the triangles are calculations based on the chemical composition of real tissues.

Previous work has been reported concerning the influence of all these errors. Chen et al. (1979) measured the Bragg-peak-shift in one abdomen slice of the Alderson phantom and compared this result with the range calculation based on their CT calibration. They obtained differences between measurement and calculation of about 5 % of the traversed matter. However, the abdomen is not the most critical region. We expect bigger errors, for example, in head regions where a lot of bone structures and high-low density interfaces are present. Alpen et al. (1985) also measured the Bragg-peak-shift of a neon and a helium beam in a frozen dog for seven selected target locations. They obtained errors of up to 11 % between CT range and measured range. They concluded that big deviations appeared where bone or air filled cavities were in the beam path.

In the next section we will present measurements of the proton range in biological tissue obtained using our radiographic equipment and will compare them with the calculation based on CT calibration by tissue substitutes.

3.7.2 Range measurements and calibration check

The sheep's head was scanned using the described radiographic apparatus and the integral density of the matter traversed by the protons was measured experimentally. The mean range in every pixel was calculated to be the 50 % fall-off of the integrated range spectrum. For the corresponding range calculation, the calibrated CT data were integrated in the direction of the proton beam to produce projections transverse to the beam. The DRR's are supposed to contain the same information as the measurements. The algorithm used to compute the DRR's was the same as the one used in the PSI treatment planning system to calculate the position of the Bragg peak for the dose calculation. The goal of these comparisons is to quantify the different sources of range errors.

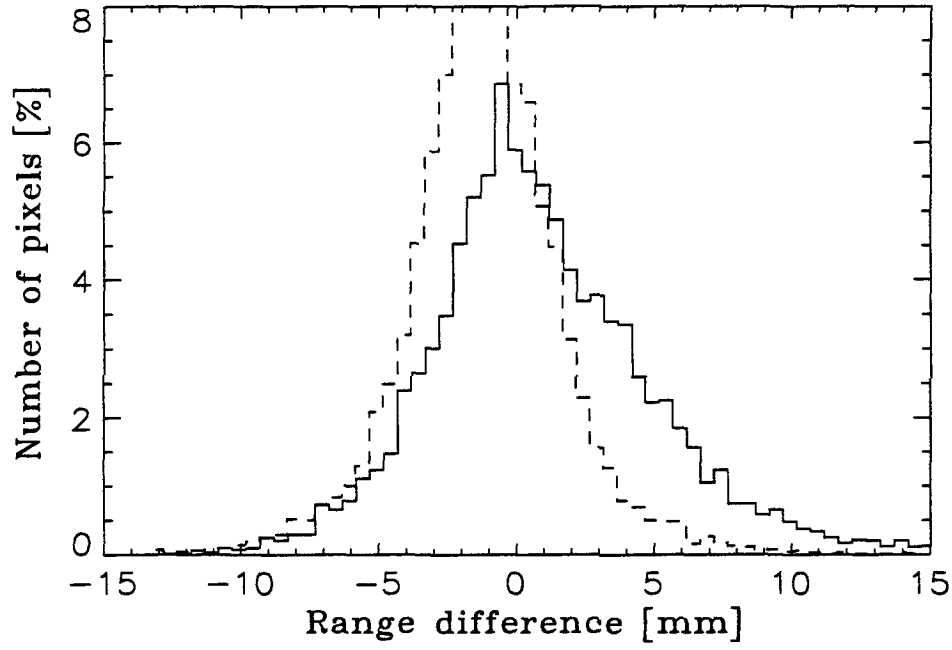

Figure 24 Histogram of range differences between DRR and proton radiography ($\Delta r = r_{DRR} - r_{radiography}$). The plot shows the number of pixels as a function of their range difference, the solid line for the tissue-substitute-calibration and the dashed line for the stoichiometric-calibration.

Figure 24 shows a histogram of the range differences between prediction and measurement (Δr) in the sheep's head using our tissue substitute calibration (solid line). The proton image of the sheep's head is shown in figure 31. The different colours in this figure indicate range differences (red: $|\Delta r| > 7$ mm, blue: 7 mm > $|\Delta r| > 2.5$ mm, yellow: 2.5 mm > $|\Delta r| > 0.7$ mm). As can be seen from figure 31, remarkable differences are found in the regions containing bone structures, especially in the region of the mastoid air cells (processus mastoideus, bulla tympanica) and the brain. Other problems are the region around the eye, which produces stopping power higher than estimated by the

calibration, and the region behind the tongue, which gives Hounsfield values like muscle tissue (999) but results in higher relative stopping powers.

To improve the range calculation, we varied the tissue substitute calibration of the CT-data. From the known chemical composition of the tissue substitutes and the measurements of their Hounsfield values, we could parametrise the response of the CT unit by fitting the dependence of the photon attenuation as a function of the atomic number of the elemental composition of these materials (see Appendix B). Using this model and tissue descriptions from Allisy (1988), Constantinou (1974) and Mustafa and Jackson (1983) we determined then Hounsfield values for "real biological tissues" (table 4). The corresponding relative stopping power was calculated with the Bethe Bloch formula (28). A linear curve, shown as the dotted line in figure 23, has been fitted through the calculated data points for brain, blood, soft bone, compact bone, hard bone and bone mineral. The range differences between calculation and measurement for this "stoichiometric CT calibration" are shown as the dotted line in figure 24. The maximum deviation could be reduced from 23 mm to 16 mm and the mean deviation from 3.7 mm to 2.7 mm. This result implies that a direct calibration based on measurements with tissue substitutes is not appropriate for obtaining the best results.

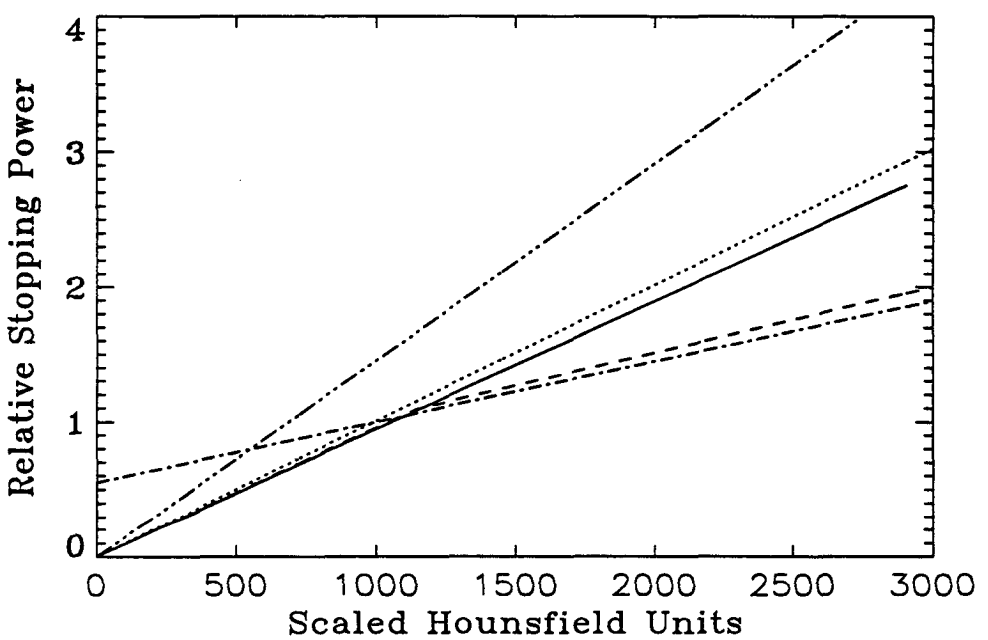

Figure 25 Different organ-calibrations from Hounsfield values to relative proton stopping power. The solid line represents the calibration for the eyes, the dotted line for brain tissue, the dashed line for non spongiosa bone, the dashed-dotted line for the nasal cavity and the dashed-dotted-dotted line for the region behind the tongue.

One remaining problem is that different organs and tissues have different relative stopping powers for the same Hounsfield value in the CT-slices due to their different chemical composition. This problem cannot be solved with a single calibration curve for the whole body. A possible solution is to use different calibrations for different organs. To investigate this we segmented the CT-cube of the sheep into various organs, like the brain, the eyes, the mastoid air cells with surrounding bone, the nasal cavity and the region behind the tongue, and calibrated the voxels for different organs with different calibration curves. Figure 25 shows these organ specific calibrations. The calibrations for the eyes and the brain were produced by taking the corresponding calculated values of the stopping power and mixing them with air to model different densities in these organs. The mastoid air cells were modelled as a mixture of air and calculated bone values. In the nasal cavity, bony structures are generally small and it has been assumed that the voxel values here are a mixture between bone, nasal secretion which is mainly water, and blood. For the region behind the tongue the measurement shows a systematic shift compared to the calculation. We do not have an explanation for this behaviour and could solve this problem only by assuming a high stopping power (= 1.45) for this region which corresponds to Hounsfield values comparable to muscle (~ 1000).

Table 1 Deviation between calculated DRR and measured proton radiography in mm for different organs.

Region of the sheep's head	Maximum deviation in mm / RMS deviation in mm		
	Tissue substitute calibration	Stoichiometric calibration	Organ specific calibration
Total head	23.0 / 3.7	15.5 / 2.7	13.9 / 2.6
Brain	13.9 / 4.1	7.9 / 2.2	2.7 / 1.3
Eyes	10.1 / 2.9	5.7 / 2.0	5.6 / 2.0
Mastoid air cells and surrounding bone	23.0 / 7.4	14.1 / 3.9	8.2 / 2.6
Nasal cavity	13.0 / 2.9	5.6 / 1.9	5.6 / 1.9
Region behind the tongue	8.8 / 6.0	9.7 / 7.3	7.3 / 3.0
Lateral field for the irradiation of a brain tumour	13.1 / 3.2	6.8 / 2.1	2.9 / 1.2
Homogeneous moulage material	2.3 / 0.6	2.3 / 0.6	2.3 / 0.6

After this procedure, DRRs were again produced and compared to the measurements. The deviations in the regions of the segmented organs were strongly reduced. The

mean deviation in the region behind the tongue diminished from 7.3 mm for the stoichiometric calibration to 3.0 mm for the organ specific calibration. The region of the brain improves from 2.2 mm mean deviation to 1.3 mm and the range error of the mastoid air cells decreases from 3.9 mm to 2.6 mm. Table 1 summarises the different calibrations and their range errors. We have also included in the table those values where protons passed through homogeneous moulage material to get an idea of the precision of the measurement.

It is important to note that in a practical situation, only the region covered by the incident beam used for therapy is relevant for the precision of treatment. To simulate a clinical situation we have chosen as an example a supposed brain tumour to be irradiated from the lateral direction. The chosen field is shown in figure 31. The range differences corresponding to different calibrations are shown for the reduced region of the field in table 1. From these, it is possible to calculate the deviation per mm through the whole sample and hence calculate the deviation at any given depth. For a distal tumour boundary with 100 mm distance to the surface, the maximum deviation using the tissue substitute calibration is 10.3 mm and the RMS deviation is 2.5 mm. If the organ specific calibration is used to calculate the DRR, the maximum deviation in the chosen field is diminished to 2.3 mm and the RMS-value to 0.9 mm which is in the order of the positioning precision.

Table 2 Deviation between calculated DRR and measured proton radiography in mm for different organs for voxels where the spectral range uncertainties are smaller than 4.9 mm.

Region of the sheep's head	**Maximum deviation in mm / RMS deviation in mm**		
	Tissue substitute calibration	**Stoichiometric calibration**	**Organ specific calibration**
Total head	11.0 / 2.0	6.9 / 1.8	6.9 / 1.7
Brain	4.2 / 1.9	3.2 / 1.7	2.1 / 1.1
Eyes	5.3 / 2.4	4.6 / 1.7	4.5 / 1.9
Mastoid air cells and surrounding bone	5.8 / 2.4	4.0 / 2.5	2.9 / 2.1
Nasal cavity	6.2 / 2.0	4.6 / 1.7	4.6 / 1.7
Region behind the tongue	7.4 / 5.8	8.3 / 6.9	5.2 / 2.8
Lateral field for the irradiation of a brain tumour	11.1 / 2.5	6.0 / 1.9	2.3 / 1.0
Homogeneous moulage material	2.3 / 0.6	2.3 / 0.6	2.3 / 0.6

As we mentioned in the last section, irradiation fields should be chosen in such a way as to have low range uncertainties in the field. The range uncertainties also affect the precision of calculating the mean range. For wide range deviations the resulting spectra becomes non-gaussian and thus measurements of the mean range become less precise. Hence in table 2 the deviations of prediction and measurement are listed for those voxels which belong to range uncertainties lower than 4.9 mm. The difference between measurement and calculation shows the same behaviour as for voxels without range uncertainty limitation, i.e. the stoichiometric and the organ specific calibration represent an improvement to the tissue substitute calibration.

We conclude that a precise check of the calculated range is important for precise proton treatments. Proton radiography can help to find better calibrations for CT-data and so to reduce errors in the calculated dose distributions for therapy. Clearly more experiments have to be done in order to confirm the practical value of the solution proposed here as a first result of these preliminary studies.

3.8 Discussion and outlook

It has been shown that proton radiography is a useful tool for quality control purposes in proton therapy. The dose distribution for stopping protons, calculated on the basis of range calculations, can be indirectly checked with range measurements of transmitted protons. Measurements of range uncertainties due to inhomogeneities in the patient can indicate critical situations. As a consequence, the angle of irradiation may be changed or the safety margin around the target volume be defined on the basis of these measurements. To guarantee a very precise irradiation, the optimal strategy is to outline individual organs in the CT data and apply organ specific calibrations to the data to eliminate the effects due to different chemical compositions. This could be a reasonable approach if organs are anyhow already outlined for performing complication probability calculations of treatments. On the basis of these measurements the calibration from Hounsfield values to relative proton stopping power can be verified and safety margins can be derived for each treatment field. In addition a positioning check with proton images is possible.

Proton radiographies of each treated patient could be used as documents to prove the accuracy of each individually applied proton treatment. Due to the low dose given with proton radiography this could be done for each fraction and could be used to detect changes of the anatomy during treatment, for example a decrease of the tumour volume, loss of patient weight or similar effects.

The experimental set-up used for this feasibility study had the disadvantage of a low data acquisition rate (1000 protons per second). This was not important for these preliminary studies but will be important for the use of proton radiography with patients.

This low rate was due to three main reasons. Firstly the movement of the range shifter is slow (~100 ms), secondly the NaI crystal is difficult to operate at MHz event rates and finally the data transfer from the Starburst to the VAX station was slow (1 kHz).

As a next step, we plan to develop a fast radiographic system which can be used with patients. For our future system we propose to measure the proton range with a range telescope (a stack of plastic scintillators). With a resulting dynamic range of 20 cm the range shifter has to be used very rarely. Since plastic scintillators have a fast rise and fall time (~20 ns), rates in the order of MHz may be achieved. To accelerate the data transfer we want to load the digitised signals into a digital memory. The acquisition rate would be increased to between 100 kHz and 1 MHz in order to take images within minutes.

Appendix A. Estimation of the density resolution of the system

The overall energy resolution (ΔE in MeV or ΔR in cm) of our proton radiographic experiments include detector resolution (ΔE_{NaI} or ΔR_{NaI}), energy straggling of the initial beam due to its momentum band (ΔE_{mom} or ΔR_{mom}) and energy straggling due to the statistical energy loss of protons passing through matter (ΔE_{str} or ΔR_{str}). For the following estimation of energy and density resolution we use a simple dependence of energy and range (Leo 1994):

$$E = (aR + b)^{\frac{4}{7}} \qquad (30)$$

where E and R are energy and range of the protons in MeV and cm respectively and a=405.53 and b=5.24 are constants determined by a fit of formula (30) to the Janni data table (Janni 1982).

For stopping protons of a given initial energy the range straggling ΔR is a constant. Range straggling due to energy loss is then given by:

$$\Delta R_{str} = 0.33cm \quad for \quad E_0 = 218.2\,MeV \qquad (31)$$

where E_0 is the initial energy of the protons. We assume that a change in range ($R+\Delta R$) corresponds to a change in the energy ($E+\Delta E$) measured by the detector. Using formula 30 we get for the corresponding variations of the measured energy straggling in the detector

$$\Delta E_{str} = \frac{dE}{dR}\Big|_E \Delta R_{str} = \frac{a}{1.75} E^{-\frac{3}{4}} \Delta R_{str} \equiv \varphi E^{-\frac{3}{4}}, \qquad (32)$$

where E is the residual energy measured by the NaI-crystal and φ contains all the energy independent terms. Range straggling due to the momentum band of the beam is determined from the uncertainty of the initial energy (ΔE_0):

$$\Delta R_{mom} = \frac{\Delta E_o}{\frac{dE}{dR}\Big|_{E_o}} \equiv \mu \quad and \quad \Delta E_{mom} = \Delta R_{mom} \frac{dE}{dR}\Big|_E \equiv \xi E^{-\frac{3}{4}} . \qquad (33)$$

The energy resolution of the NaI crystal is proportional to the square root of the residual energy of the protons. Thus we get

$$\Delta E_{NaI} = \kappa E^{\frac{1}{2}} \quad and \quad \Delta R_{NaI} = \nu E^{\frac{5}{4}}. \qquad (34)$$

The total energy straggling is given by

$$\Delta E = \sqrt{\varphi^2 E^{-\frac{3}{2}} + \xi^2 E^{-\frac{3}{2}} + \kappa^2 E} \; . \qquad (35)$$

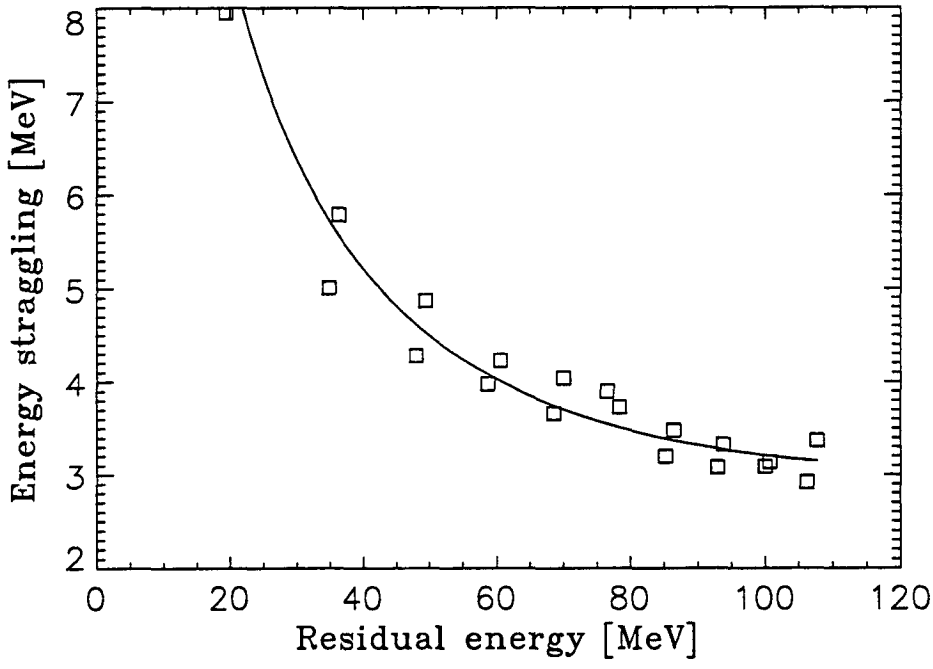

Figure 26 Plot of the error ΔE in the energy measurement as a function of the measured residual energy E. The solid line is a fit to the measured values (symbols).

With the knowledge of the initial beam energy and range straggling we calculate φ = 76.2. A fit of formula 35 to the experimental data (figure 26) yields the unknown constants ξ = 26.1 and κ = 0.2 respectively. The determined constants correspond to a momentum band $\Delta p/p$ = 0.6 % (FWHM) and a detector resolution of 1.6 MeV for 60 MeV residual energy. These values are close to the ones which can be found in the literature (Leo 1994, Salmieri et al. 1986, Scheib 1994).

Appendix B. Calculation of the CT numbers and relative stopping powers

A CT image represents the spatial distribution of photon attenuation coefficients. The scaled Hounsfield number is defined by

$$H = 1000\frac{\mu}{\mu_w} \tag{36}$$

where μ is the linear attenuation coefficient of the material and μ_w the coefficient for water. There are two effects which lead to the attenuation of a photon beam for energies up to 1 MeV energy (below the threshold of pair production), photoelectric absorption and scattering. The cross section of scattering processes can be divided into that due to incoherent scattering (compton scattering defined as free electron scattering) and coherent scattering (Rayleigh scattering with a correction term to account for deviations due to binding energy effects). The total attenuation coefficient can be written in the form (Jackson and Hawkes 1981)

$$\mu = \rho N_g(Z,A)\left\{\sigma^{ph} + \sigma^{coh} + \sigma^{incoh}\right\} \tag{37}$$

where ρN_g is the electron density and σ^{ph}, σ^{coh}, σ^{incoh} the cross sections for photoelectric effect, coherent scattering and incoherent scattering respectively. An accurate parametrisation of those cross sections is given by Rutherford et al. (1976)

$$\mu = \rho N_g(Z,A)\left\{K^{ph}E^{-3.28}Z^{3.62} + K^{coh}E^{-2.02}Z^{1.86} + \sigma_e^{KN}(E)\right\} \tag{38}$$

where $K^{ph}$and K^{coh} are constants which characterise the different cross sections and $\sigma_e^{KN}(E)$ is the Klein-Nishina cross section for photons of energy E. For a mixture of elements the attenuation coefficient can be obtained by the following formula (Jackson and Hawkes 1981)

$$\mu = \rho N_g(Z,A)\left\{K^{ph}E^{-3.28}\tilde{Z}^{3.62} + K^{coh}E^{-2.02}\hat{Z}^{1.86} + \sigma_e^{KN}(E)\right\} \tag{39}$$

where

$$\tilde{Z} = \left[\sum \lambda_i Z_i^{3.62}\right]^{\frac{1}{3.62}} \tag{40}$$

$$\hat{Z} = \left[\sum \lambda_i Z_i^{1.86}\right]^{\frac{1}{1.86}} \qquad (41)$$

and

$$\lambda_i = \frac{N_g^i}{N_g} \qquad (42)$$

where N_g is the number of electrons per unit volume of the mixture given by

$$N_g = \sum N_g^i = N_A \sum \frac{\omega_i Z_i}{A_i} \qquad (43)$$

where N_A is Avogadro's number, Z_i and A_i are, respectively, the atomic number and atomic weight of the i-th element and ω_i is its proportion by weight.

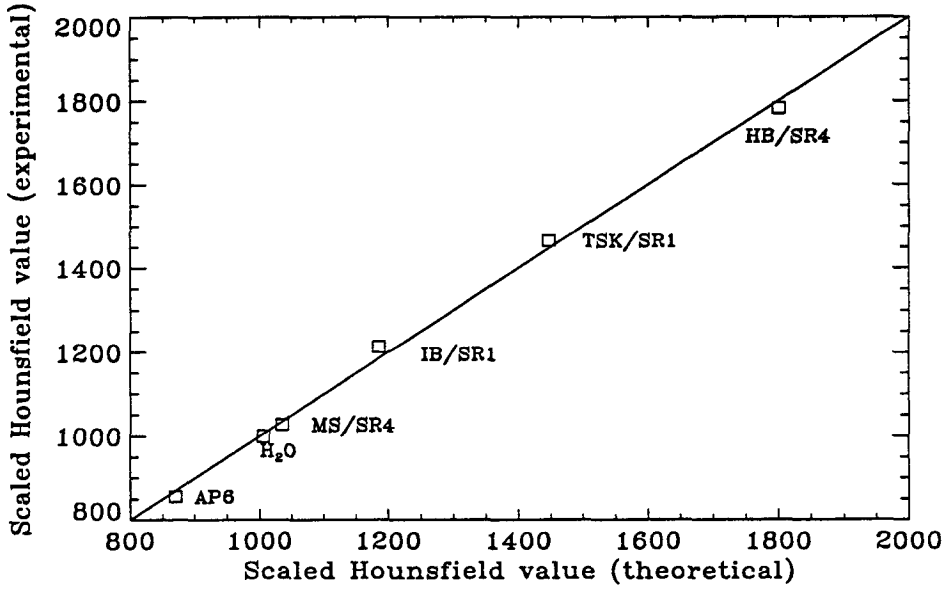

Figure 27 Experimental Hounsfield values versus calculated Hounsfield values with formulae 39 and 36.

By making measurements of H for different tissue substitutes of known chemical composition (table 3) with the fixed energy of 120 kVp (80 kV) we can determine from a linear regression fit of the experimental data to formulae 39 and 36 the constants

K^{ph} and K^{coh} to be 20.1 and 2.80 respectively. With the knowledge of these constants and the chemical compostion of different biological tissues (Allisy 1983, Mustafa and Jackson 1983, Kijewski and Bjärngard 1978) we can calculate their Hounsfield numbers (table 4). The calculated ratios of stopping power to Hounsfield values for the real tissues are lower compared to tissue substitutes due to the fact of higher carbon and less calcium content in tissue substitutes.

One should bear in mind that the chemical composition of different tissues extracted from the literature are just approximations and this inevitably induces errors in the Hounsfields number and hence stopping power calculation.

Table 3 Chemical composition (percentage weights) of various tissues and tissue substitutes.

	H	C	N	O	F	Na	Mg	P	S	Cl	K	Ca
atomic number	1	6	7	8	9	11	12	15	16	17	19	20
atomic weight	1.0079	12.011	14.006	15.999	18.998	22.989	24.312	30.973	32.064	35.450	39.102	40.080
Material	composition in % of weight											
AP 6	8.36	69.14	2.36	16.94	3.07					0.14		
water	11.19			88.81								
MS/SR 4	9.5	70.25	3.48	15.15		0.08	0.02	0.18	0.50	0.12	0.30	0.01
IB/SR 1	8.73	63.19	2.36	17.83		0.06		2.62		0.12		5.09
TSK/SR 1	6.4	46.4	2.80	26.4		0.30	0.10	7.0	0.20	0.10	0.20	10.0
HB/SR 4	4.45	29.09	3.88	31.93		0.06	0.21	10.0	0.32	0.06		19.99
fat	12.21	76.08		11.71								
lung	9.9	10.0	2.8	74.0				0.1			0.2	
lung 2	9.7	70.26	2.8	16.3		0.17	0.01	0.12	0.22	0.11	0.19	0.01
muscle	10.2	12.3	3.5	72.9		0.08	0.02	0.2	0.5		0.3	0.007
soft bone	8.67	13.0	3.6	66.4		0.08	0.06	2.43	0.46		0.23	4.96
compact bone	6.4	27.8	2.7	41.0			0.2	7.0	0.2			14.7
hard bone	3.39	15.5	3.97	44.1		0.06	0.21	10.2	0.31			22.2
teeth	2.2	9.3	2.8	41.3	0.008		0.7	13.5				28.3
brain	11.07	12.54	1.33	73.78		0.18	0.015	0.35	0.18	0.24	0.31	0.009
blood	10.2	10.0	3.0	76.2		0.19		0.04	0.19		0.16	
bone mineral	0.2			41.4				18.5				39.9

The stopping power was calculated according to Bethe-Bloch's formula (28). The ionisation energy I_i for each element was taken from Janni (1982) and the mean ionisation energy for a mixture was calculated using the Bragg additivity rule

$$\ln I_m = \frac{\sum \frac{\omega_i Z_i}{A_i} \ln I_i}{\sum \frac{\omega_i Z_i}{A_i}} \qquad (44)$$

The results are shown in comparison to the experimental values in table 4.

Table 4 Measured and calculated Hounsfield numbers and stopping powers for different materials.

Material	Density in g cm^{-3}	relative electron density	Hounsfield number experimenta	Hounsfield number theorical	relative stopping power experimental	relative stopping power theoretical
AP 6	0.91	0.885	856	865	0.87	0.90
water	1.00	1.00	1000	1000		1.00
MS/SR 4	1.07	1.049	1027	1029	1.07	1.08
IB/SR 1	1.15	1.123	1214	1179	1.14	1.14
TSK/SR 1	1.32	1.259	1466	1440	1.27	1.26
HB/SR 4	1.48	1.386	1783	1791		1.35
fat	0.91	0.918		906		0.95
lung	0.30	0.288		288		0.29
lung2	0.41	0.404		395		0.42
muscle	1.0	0.991		993		0.99
soft bone	1.12	1.093		1171		1.09
compact bone	1.7	1.623		1958		1.60
hard bone	1.85	1.715		2282		1.65
teeth	2.17	1.950		2806		1.85
brain	1.03	1.028		1031		1.03
blood	1.06	1.051		1051		1.05
bone mineral	3.2	2.869		4649		2.66

Appendix C. Reconstruction of the images

C.1 Fast reconstruction

For the calculation of the pixel addresses of images located at different depths, first the proton entrance (x_1,y_1) and exit (x_2,y_2) coordinates for each proton were measured by the MWPCs. Four coordinates are available to reconstruct the two coordinates for the image pixel address (x_i,y_i). The calculation of the pixels is depicted in figure 28. For each entrance and exit coordinate the most probable proton trajectory was calculated

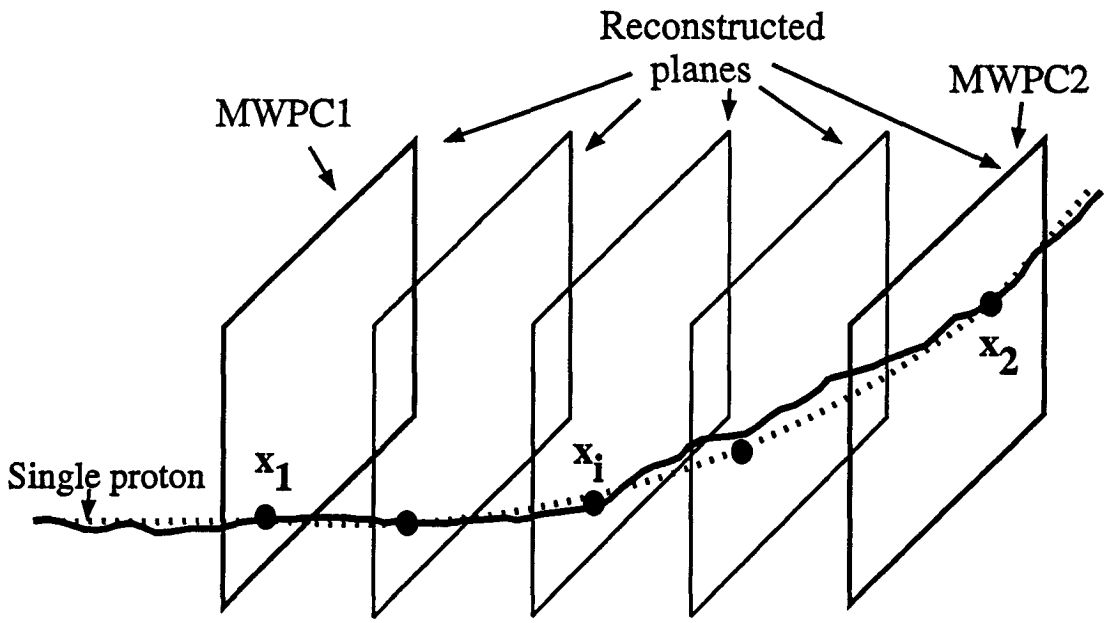

Figure 28 Scheme of the reconstruction of pixel addresses in different depths of the patient. At five depths between the two multiwire proportional chambers the pixels addresses were calculated with the knowledge of the most probable proton trajectory (dotted line) which is an approximation to the real proton path (solid line).

with formula 23. The intercept coordinates of the proton trajectory with 5 equally spaced parallel planes between MWPC1 and MWPC2 were used as pixel addresses of the image reconstructed at different depths. This reconstruction was done to better resolve structures located at the depth of the calculated image.

The residual energy of the protons was added to the histogram of energies for each pixel. After this was done for all protons, the energy (or range) spectra of each pixel was evaluated in different ways. The pixel value may be determined for example by simply averaging the energies (or ranges), by fitting a Gaussian to the spectra or by integrating the spectra and taking the 50 % fall off as the resulting pixel value for the images to be reconstructed. The last method was chosen for the presentation of the results of this experiment.

C.2 Backprojection algorithm

Another possibility to reconstruct the images in different depths is to use an iterative backprojection algorithm. Again the most probable proton trajectory with intercepts (x_i,y_i) is calculated for each proton. We assume that the five planes contain the density information for a layer at that depth. We determine then the difference between the measured residual energy E of the proton and the sum of the pixel values of image I_i^m of the last iteration over this track (x_i,y_i). This difference is equally distributed among the involved pixel addresses (x_i,y_i) and written to a correction matrix C_i, for each plane to be reconstructed:

$$C_i(x_i,y_i) = \frac{1}{k}\left(E - \sum_i I_i^m(x_i,y_i)\right) , \qquad (45)$$

where k is the number of planes, i denotes the i-th plane and m the m-th iteration. These corrections are cumulated for all protons. The image for the next iteration step is then created by adding the correction matrix normalised to the number N of protons which are contained in the spectra of each pixel (x,y):

$$I_i^{m+1} = I_i^m + \frac{C_i(x,y)}{N_i(x,y)} . \qquad (46)$$

The advantage of this method compared to the fast reconstruction is an improved spatial resolution since this algorithm focuses simultaneously objects lying at different depths in one image. Unfortunately the images reconstructed in this way are correspondingly more noisy. This is probably due to the fact that the computer algorithm has more degrees of freedom to distribute individual event fluctuations into a larger number of pixels.

To illustrate the properties of the different reconstructions methods a Monte Carlo simulation of a proton radiography of a geometrical phantom was done (Tourovsky et al. 1993). Two thin plates (1.7 mm) of very dense material were simulated in a homogeneous water bath, one plate located in the entrance plane and one in the exit plane. Figure 29 shows the reconstructed images of a simulated radiography taken in a direction perpendicular to the two planes. Images A, B and C were created with the fast reconstruction algorithm and image C with the backprojection algorithm, respectively. Image A is the reconstruction in the front plane of the phantom. As we expect, this image shows the front plate with sharp edges and the rear edges become blurred. Analogous, image B, which was reconstructed in the rear plane, shows the opposed behavior. Image C is the average of A and B, which shows the rear and the frontal plate with an average spatial resolution. However, the backprojection algorithm, which was used to create image D, focuses simultaneously the two plates but has the disadvantage of more noise.

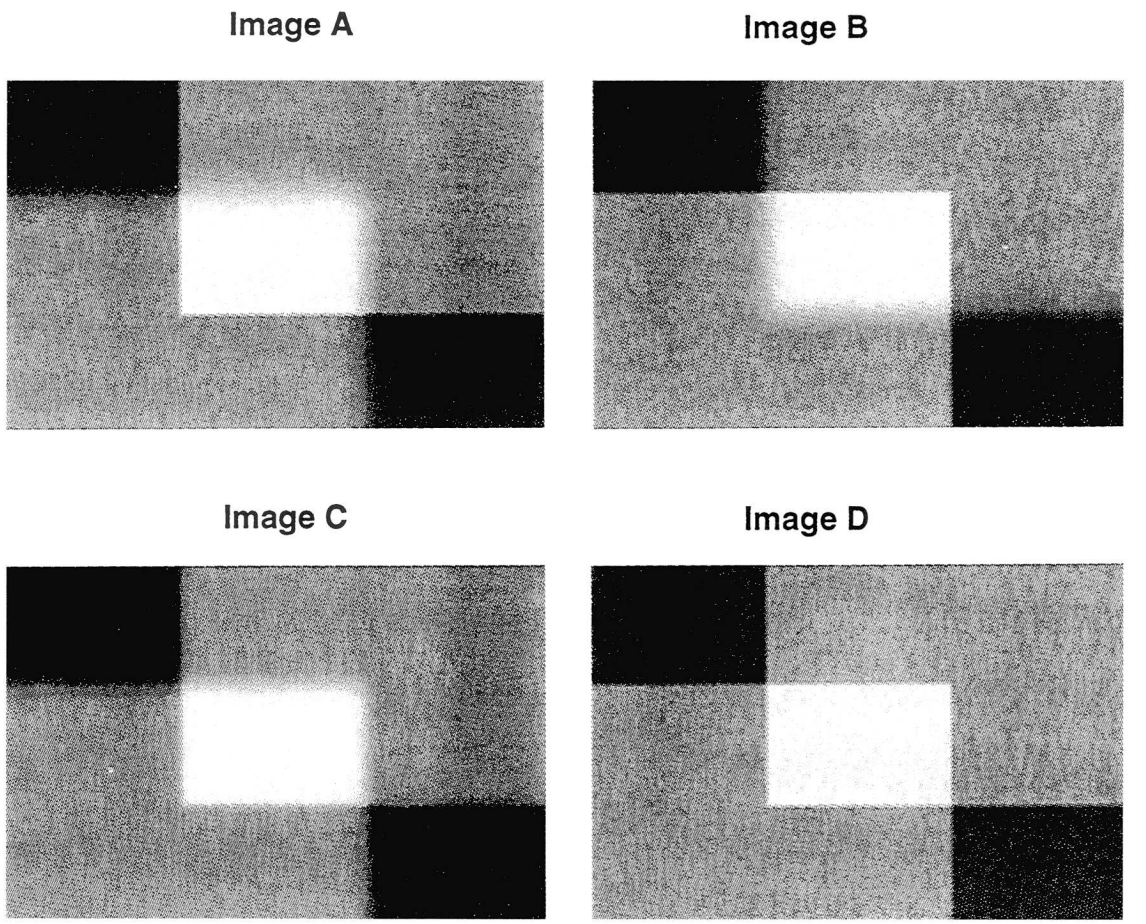

Figure 29 Illustration of two different methods of image reconstruction. The images show two thin plates of dense material immersed in the front (top right of the image) and the rear (bottom left of the image) of a water bath. The images A,B and C are the result of the fast reconstruction; A is focused in the front plane, B in the rear plane and C is the average of images A and B. Image D is the result of the backprojection reconstruction.

As the images presented in this preliminary study were produced with a small number of protons, and since the backprojection algorithm produces only the image of the mean ranges and not of the range uncertainties, we decided for this work to use the fast reconstruction method.

More work should be spent in the future in the investigation of reconstruction algorithms in order to be sure that the information contained in the radiographic data is optimally used.

Appendix D. Colour images

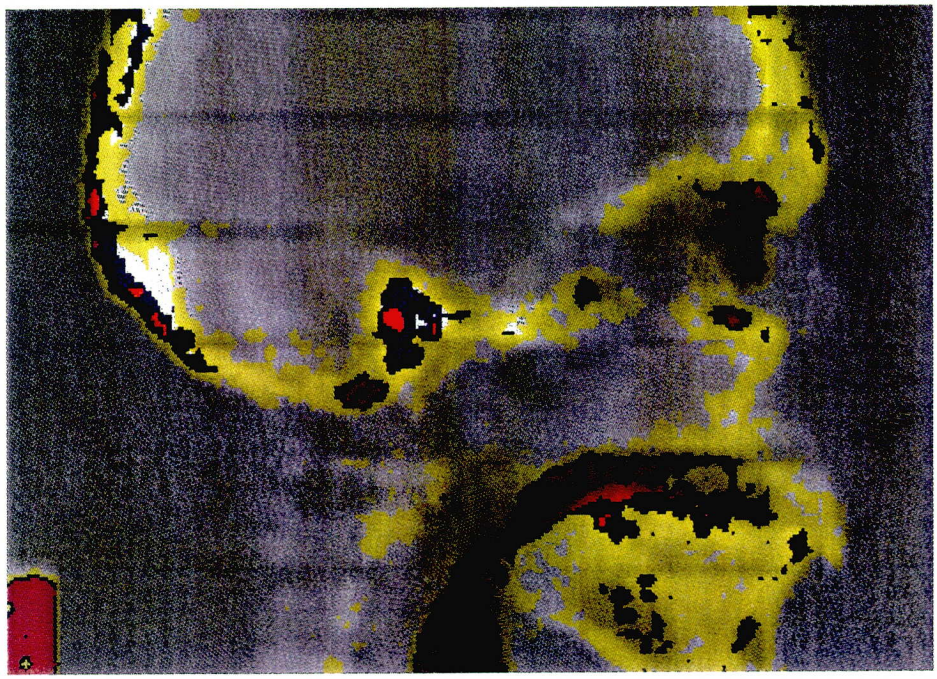

Figure 30 DRR image of the Alderson head. The colours indicate range uncertainties of the protons (red: > 15 mm, 15 mm > blue > 10 mm, 10 mm > yellow > 5 mm).

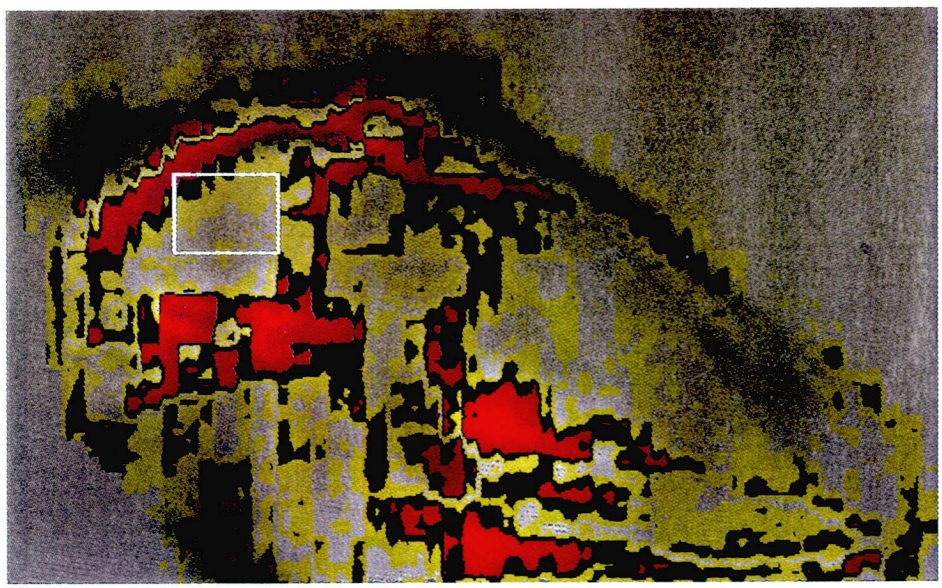

Figure 31 Proton range image of the sheep's head. The colours indicate range differences between calculated DRR and experimental proton radiography (red: $|\Delta r| > 7$ mm, blue: 7 mm > $|\Delta r| > 2.5$ mm, yellow: 2.5 mm > $|\Delta r| > 0.7$ mm). The white rectangular labels a field to be irradiated for a brain tumour.

References

M. Akisada, J. Ohashi, K. Kondo, D. Kurihara, S. Miyashita, A. Tachikawa, Y. Takada, K. Takikawa, "Conceptual Design of Proton Computed Tomography with Magnetic Spectrometer," Jap. J. of Appl. Phy. **22-4**, 752-758 (1983).

A. Allisy (editor), *Tissue Substitutes in Radiation Dosimetry and Measurement*, ICRU Report 44 (1988)

E. Alpen, D. Saunders, A. Chatterjee, J. Llacer, G. Chen, J. Scherer, "A comparison of water equivalent thickness measurements: CT method vs. heavy ion beam technique," The British Journal of Radiology **58**, 542-548 (1985).

J. O. Archambeau, G. W. Benett, G. S. Levine, R. Cowen, A. Akanuma, "Proton Radiation Therapy," Radiology **110**, 445-457 (1974).

J.J Battista, W.D. Rider, J. van Dyk, "Computed Tomography for Radiotherapy Planning," Int. J. Radiation Oncology Biol. Phys., **6**, 99-107 (1980).

J.J Battista, M.J. Bronskill, "Compton scatter imaging of transverse sections: an overall appraisal and evaluation for radiotherapy planning," Phys. Med. Biol., **26-1**, 81-99 (1981).

H. Bichsel, *Passage of charged particles through matter*, Amer. Inst. of Physics Handbook, McGraw Hill, 8-142-8-189 (1972).

H. Bichsel, K.M. Hanson, M.E. Schillaci, "Lateral displacement in small angle multiple scattering," Phys. Med. Biol. **27-7**, 959-961 (1982).

L. Brown, D. Nordstrom, S. Brown (editors), *Review of particle properties*, Phys. Rev. D, Part II (1992).

G. Chen, R. Singh, J. Castro, J. Lyman, J. Quivey, "Treatment planning for heavy ion radiotherapy," Int. J. Radiation Biol. Phys. **5**, 1809-1819 (1979).

C. Constantinou, "Tissue substitutes for particulate radiations and their use in radiation dosimetry and radiotherapy," PhD thesis, London University, 1974.

C. Constantinou, J. Harrington, "An electron density calibration phantom for CT-based treatment planning computers," Med. Phys. **19-2**, 325-327 (1992).

J.A. Cookson, "Radiography with Protons," Naturwissenschaften **61**, 184-191 (1974).

A.M. Cormack, A.M. Koehler, "Quantitative Proton Tomography: Preliminary Experiments," Phys. Med. Biol. **21-4**, 560-569 (1976).

K.M. Crowe, T.F. Budinger, J.L. Cahoon, V.P. Elischer, R.H. Huesman, L.L. Kanstei, "Axial scanning with 900 MeV alpha paricles," IEEE Transactions on Nuclear Science **NS-22**, 1752-1754 (1975).

J. Curry, V.W. Steward, "Establishment of a beam line at the Fermi National Accelerator Laboratory for proton radiography," Med. Phys. **5(3)**, 188-195 (1978).

L. Eyges, "Multiple Scattering with Energy Loss," Phys. Rev. **74**, 1534-1535 (1948).

F.J.M. Farley, P. Mandrillon, "High Energy Accelerators in Medicine," Europhysics News **23-1**, 1-20 (1992).

R.A. Geise, E.C. McCullough, "The use of CT Scanners in Megavoltage Photon-Beam Theraphy Planning," Radiology **124**, 133-141 (1977).

M. Goitein, "The Measurement of Tissue Heterodensity to guide charged Particle Radiotherapy", Int. J. Radiation Oncology Biol. Phys. **3**, 27-33 (1977).

M. Goitein, J.M. Sisterson, "The Influence of Thick Inhomogeneities on Charged Particle Beams", Radiation Research **74**, 217-230 (1978a).

M. Goitein G.T.Y. Chen, J.Y. Ting, R.J. Schneider, J.M. Sisterson, "Measurements and calculations of the influence of thin inhomogeneities", Med. Phys. **5-4**, 265-273 (1978b).

M. Goitein, "Calculation of the uncertainty in the dose delivered during radiation thaerapy", Med Phys. **12-5**, 608-612 (1985).

K.M. Hanson, J. N. Bradbury, T.M. Cannon, R.L. Hutson, D.B. Laubacher, R.J. Macek, M.A. Paciotti, C.A. Taylor, "Computed tomography using proton energy loss," Phys. Med. Biol. **26/6**, 965-983 (1981).

K.M. Hanson, J.N. Bradbury, R.A. Koeppe, R.J. Macek, D.R. Machen, R. Morgado, M.A. Paciotti, S.A. Sandford, V.W. Steward, "Proton computed tomography of human specimens," Phys. Med. Biol. **27/1**, 25-36 (1982).

D.J. Hawkes, D.F. Jackson," An accurate parametrisation of the attenuation coefficient", Phys. Med. Biol. **25-6**, 1167-1171 (1980).

V.L. Highland, "Some practical remarks on multiple scattering," Nucl. Inst. and Meth. **129**, 497-499 (1975) and "Erratum," Nucl. Inst. and Meth. **161**, 171 (1979).

D.F. Jackson, D.J. Hawkes, "X-ray attenuation coefficients of elements and mixtures," Physics Reports **70-3**, 169-233 (1981).

J.F. Janni," Proton range-energy tables," Atomic Data and Nucl. Data Tables **27**, 212-425 (1982).

H.E. Johns, J.R. Cunningham, *The physics of radiology*, 4th ed., Charles C. Thomas, Springfield, Illinois, USA (1983).

P.K. Kijewski, B.E. Bjärngard, "The use of computed tomography data for radiotherapy dose calculations", Int. J. Radiation Oncology Biol. Phys. **4**, 429-435 (1978).

A. M. Koehler, V.W. Steward, " Proton Radiographic Detection of Strokes," Nature **245**, 38-40 (1973a).

A.M. Koehler, V.W. Steward," Proton Beam Radiography in Tumor Detection," Science **179**, 913-914 (1973b).

W.R. Leo, *Techniques for Nuclear and Particle Physics Experiments*, 2th ed., Springer-Verlag Berlin (1994).

G.R. Lynch, O.I. Dahl," Approximation to multiple Coulomb scattering," Nucl. Inst. and Meth. **B58**, 6-10 (1991).

E. C. McCullough, T.W. Holmes, "Acceptance testing computerized radiation therapy treatment planning systems: Direct utilization of CT scan data," Med. Phys. **12-2**, 237-242, (1985).

R.H. Millar, "Experimental X-ray Attenuation Coefficients at Low Photon Energies for Substances of Medical importance", Phys. Med. Biol. **20-6**, 974-979 (1975).

D.R. Mofett, E.P. Colton, E.W. Concaildi, E.W. Hoffman, R.D. Klem, M.J. Knott, S.L. Kramer, R.L. Martin, E.F. Parker, A.R. Passi, P.F. Schultz, R.L. Stockley, R.E. Timm, "Initial test of a proton radiographic system," IEEE Transactions on Nuclear Sciences **NS-22/3**, 1749-1751 (1975).

M. Moyers, D. Miller, J. Siebers, R. Galindo, S. Sun, M. Sardesai, L. Chan, "Water Equivalence of Various Materials for 155 to 250 MeV Protons," submitted to Medical Physics in 1993.

A. Mustafa, D. Jackson, "Small-angle multiple scattering and spatial resolution in charged particle tomography," Phys. Med. Biol. **26**, 461-472 (1981).

A. Mustafa, D. Jackson, "The relation between x-ray CT numbers and charged particle stopping powers and its significance for radiotherapy treatment planning," Phys. Med. Biol. **28**, 169-176 (1983).

E. Newman, F.E. Streigert, "Response of NaI(Tl) to Energetic Heavy Ions", Physical Review **118-6**, 1575-1578 (1960).

Øverås H.: 1960, "On small angle multiple scattering in confined bodies," CERN Yellow Report **60-18** (1960).

E. Pedroni et al., "Proton therapy project status reports," PSI Life Sciences Newsletter ,Paul Scherrer Institute, Würenlingen und Villigen, CH-5232 Villigen-PSI, Switzerland, 1989-1993 .

E. Pedroni, H. Enge, "Beam optics design of a compact gantry for proton therapy," submitted to Medical and Biological Engineering & Computing in 1993.

E. Pedroni, R. Bacher, H. Blattmann, T. Böhringer, A. Coray, A. Lomax, S. Lin, G. Munkel, S. Scheib, U. Schneider, A. Tourovsky, "The 200 MeV proton therapy project of PSI: conceptual design and practical realization," submitted to Medical Physics in 1994.

Ch. Perret, "Materialproben für CT-Eichung," PSI: Internal report **AN-64-05**, 1-5 (1980).

Ch. Perret, "Patientenmoulagen für Körper, Glieder und Hals," PSI: Internal report **AN-64-08**, 1-15 (1982).

M.E. Phelps, E.J. Hoffmann, M.M. Ter-Pogossian, "Attenuation Coefficients of Various Body Tissues, Fluids, and Lesions at Photon Energies of 18 to 136 keV," Radiology **117**, 573-583 (1975).

B. Rossi, K. Greisen, "Cosmic-ray theory," Rev. Mod. Phys. **13**, 240-268 (1941).

B. Rossi, *High Energy Particles*, Prentice-Hall, Inc., Englewood Cliffs, NJ (1965).

R.A. Rutherford, B.R. Pullan, I. Isherwood, "Measurement of Effective Atomic Number and Electron Density Using an EMI Scanner", Neuroradiology **11**, 15-21 (1976).

L. Salmieri, R. Bassini, A. Bracco, I. Iori, A. Moroni, "Comparison of the BGO and CsI(Tl) energy resolution for p and α," Nucl. Inst. Meth. in Phys. Res. **A251**, 410-411 (1986).

S. Scheib, "Spot-Scanning mit Protonen: Experimentelle Resultate und Therapieplanung," PhD thesis: Eidgenössische Technische Hochschule Zürich, Switzerland, 1994.

S. Scheib, E. Pedroni, H. Blattmann, T. Böhringer, A. Coray, A. Lomax, S. Lin, G. Munkel, U. Schneider, A. Tourovsky, "Spot scanning with protons at PSI: first experimental results on the horizontal beam line," submitted to Medical Physics in 1994a.

S. Scheib, E. Pedroni, "Spot scanning with protons at PSI: physical dose model and treatment planning," submitted to Medical Physics in 1994b.

U. Schneider, E. Pedroni, "Multiple Coulomb Scattering and Spatial Resolution in Proton Radiography," accepted for Medical Physics: June 23, 1994.

U. Schneider, E. Pedroni, "Proton Radiography as a Tool for Proton Therapy in Quality Control," submitted to Medical Physics in 1994.

P.C. Shrimpton, "Electron density values of various human tissues: in vitro Compton scatter measurements and calculated ranges," Phys. Med. Biol. **26-5**, 907-911 (1981).

W. Snyder (editor), *Report of the Task Group on Reference Man,* ICRP publication No. 23, Pergamon Press Ltd., Oxford (1975).

E. Storm, H.I. Israel, "Photon cross sections from 1 keV to 100 MeV for elements Z=1 to Z=100," Nuclear Data Tables **A7**, 565-681 (1970).

Y. Takada, I. Abe, "Multiple pencil beams for proton computed tomography," Nuclear Instruments and Methods in Physics Research **A262**, 511-521 (1987).

C.A. Tobias, E.V. Benton, M.P. Capp, A. Chatterjee, M.R. Cruty, R.P. Henke, "Particle Radiography and Autoactivation", Int. J. Radiation Oncology Biol. Phys., **3**, 35-44 (1977).

A. Tourovsky, E. Pedroni, U. Schneider, "Monte Carlo Codes for Proton Radiography and Treatment Planning (Status Report)," PSI Life Sciences, Annual Report **Annex II**, 20-22 (1993).

M. Urie, M. Goitein, W. Holley, G. Chen, "Degradation of the Bragg peak due to inhomogeneities," Phys. Med. Biol. **31**, 1-15 (1986).

Wm. J. Veigele, "Photon cross sections from 0.1 keV to 1 MeV for elements Z=1 to Z=94", Atomic Data Tables **5**, 51-111 (1973).

S. Vynckier, D.E. Bonett, D.T.L. Jones, "Code of practice for clinical proton dosimetry," Radiotherapy and Oncology **20**, 53-63 (1991).

D.R. White, "An Analysis of the Z-dependence of Photon and Electron Interactions", Phys. Med. Biol. **22**, 219-228 (1977).

D.R. White, "Tissue substitutes in experimental radiation physics", Med. Phys. **5-6**, 467-479 (1978).

H.C. Woodard, "The elementary composition of human cortical bone", Health Physics **8**, 513-517 (1962).

Acknowledgements

An dieser Stelle möchte ich mich bei all denjenigen Personen bedanken, die zum Erfolg dieser Arbeit beigetragen haben.

Bei Prof. Max Anliker möchte ich mich dafür bedanken, daß er sehr unbürokratisch die Betreung dieser Arbeit übernommen hat. Sein großes Interesse an der Arbeit am PSI ließ die Entfernung zur ETH zu keinem Problem werden. Dr. Hans Blattmann gilt mein Dank für die Übernahme der offiziellen Betreung am PSI.

Dr. Eros Pedroni als mein Betreuer hat diese Arbeit wesentlich mitgeprägt. Er hat mir sehr viele Ratschläge gegeben und immer, wenn mir die Ideen ausgingen, hatte er neue und interessante. Ohne sein Engagement wäre diese Arbeit unmöglich gewesen.

Von Dr. Dieter Renker lernte ich alles, was ich über Experimente, in dem für mich neuen Gebiet der Teilchenphysik lernen musste. Er leihte mir viele Teile meiner Apparatur. Die eifrigen Diskussionen mit Ihm, und das Verzehren von Weisswürsten und Weissbier hielten mich, auch in den schwierigen Phasen, über Wasser.

Ohne Dr. Martin Grossmann wäre ich im Dschungel der Tandem Software verlorengegangen. Seinem Enthusiasmus verdanke ich, dass alles mit der Datennahme geklappt hat.

Ein besonderer Dank gilt Hansueli Stäuble, der immer gewusst hat wo man welches Spezialkabel in möglichst kurzer Zeit besorgen kann, immer mit Rat und Tat, ganz besonders während der Experimentierzeit, zur Seite stand und immer gewusst hat, wo es die besten "Beizen" gab ("Tiger-Lady").

Herzlichen Dank an die britische Vertretung in der Strahlenmedizin, Dr. Tony Lomax und Andrew Fielding für ausführliche Nachhilfen in der englischen Sprache ("Manconian", "Yordy-English" and Welsh), im Criquet-Spiel, ...

Und natürlich auch Dank an die "PSI-Bayern", Dieter, Reinhold, Horst, Wolf-Dietrich und Gill, die mit Bayerischem Humor und Sarkasmus die Zeit kurzweilig werden liessen.

Alle meine Mitarbeiterinnen und Mitarbeiter in der Abteilung für Strahlenmedizin, die in all den Jahren für ein gutes Arbeitsklima gesorgt haben möchte ich erwähnen: Ruth, Bruno, Andy, Doc Ueli, Rolli, Terence, Doelf, Gudrun, Lin, Emanuel und Peter. Und natürlich auch Stefan und Alexander (die in Ihrer Hilfsbereitschaft meine "2-Minuten-Fragen" mit "2-Stunden-Antworten" immer ausführlich behandelten).

Nicht vergessen will ich auch die IBT-Gruppe in Zürich. Im Speziellen gilt mein Dank für Ihre stete Hilfsbereitschaft Prof. Peter Rüegsegger, Wolfgang, Barbara und Harald.

Beim Metzgermeister Peter bedanke ich mich sehr für die Bereitstellung der Schafsköpfe.

Zu guter Letzt allen Dank, die mir den Aufenthalt in der Schweiz schön gemacht haben; ganz besonders meiner Gabriela.

Curriculum Vitae

NAME	Uwe Reinhold Schneider
DATE OF BIRTH	02.02.1964
SEX	Male
MARITAL STATUS	Single
NATIONALITY	Bavarian (German)

EDUCATION

February 1991 -	Eidgenössische Technische Hochschule (Swiss Federal Institute of Technology) Zürich and Paul Scherrer Institute PhD thesis: Proton Radiography as a Tool for Quality Control in Proton Therapy Supervisor: Prof. Dr. Max Anliker, Dr. Hans Blattmann and Dr. Eros Pedroni.
1989 - 1993	Successful completion of the training scheme of the German Society for Medical Physics for a "Medical Physicist"
1988 - 1989	University of Bayreuth, Institute of Physics Diplomawork: On the symmetric baroclinic instability Supervisor: Prof. Dr. F.H. Busse
1983 - 1988	University of Bayreuth Diploma in Physics
1974 - 1983	Gymnasium Selb Abitur
1970 - 1974	Dr.-Bogner-Schule Selb